Doctoral Dissertation

Transition and selection of behaviours influenced by extracellular geometrical cues in the ciliate, *Stentor coeruleus*

（繊毛虫ソライロラッパムシの行動遷移と細胞外幾何形状に
応じた固着場所の選択）

Graduate School of Life Science, Hokkaido University

Syun Echigoya

March 2024

Contents

Figure List

1 Abstract

Background

Protists are eukaryotic cells, almost unicellular organisms that have survived for hundreds of millions of years. These cells ubiquitously live in aquatic environments, soil environments and our bodies. Furthermore, they play key roles in the food chain and water purification; conversely, they cause red tides. Protists relate our lives from several aspects. These macroscopic phenomena result from integrating each behaviour in one cell. Various microorganism behaviours have been descriptively reported from one hundred years ago. However, quantification of the behaviours is still in progress.

In aquatic environments, ciliates are dominant constitution organisms. Cilia (hair-like organelle) on the cell surface reciprocally change the beating form and stir fluid for locomotion. Swimming ciliate *Stentor coeruleus* changes its states from swimming to anchoring for feeding, accompanied by cell deformation depending on surrounding environments. Its behavioural transition from adhering to swimming relating to an avoiding reaction has been studied, but switching behaviour from swimming to adhering has yet to be focused. Their habitats consist of various geometrical structures, such as porous media and rigid surfaces, affecting their motilities. In addition, there are heterogeneous distributions of prey and predator, and external flow affects their lives. Thus, anchoring location is essential for their living in nature. In this thesis, quantifications of the behavioural transition in *S. coeruleus* in a simple observation chamber are conducted. Then, I focused on selecting anchoring locations using several geometrical chambers.

Results

Quantification of behavioral transitions in *S. coeruleus*

Using image analysis of a long-time observation in a simple chamber, I obtained a time series of the cell shape and calculated the swimming speed and cell length. The cell states were characterized statistically from these values, and I found the different time scales of each transition.

Characterization of the transition from swimming to adhering

We can see a negative correlation between cell length and swimming speed from cone-shaped swimming cells to trumpet-shaped adhering cells. In addition, swimming trajectories occur between cone-shaped cells and trumpet-shaped cells. The shape of the cell corresponds with its motility that cone-shaped is swimming form and trumpet-shaped cell is adhering form. Close observation of membranelle (ciliary bands) reveals the difference in beating forms. It suggests that the cell changes its swimming properties by modulating the beating forms of ciliary bands.

Next, I focus on when and where the cell takes a behavioural transition from swimming to adhering. Using the microfabrication technique, I observed the behaviour in a structural chamber. In a simple chamber, the cell dominantly swims in a cone-shaped state. On the other hand, the cell takes a trumpet shape in a structural chamber compared with the simple chamber. These results indicate that a structure affects their motility and behavioural change from swimming form to adhering form. Trumpet-shaped cell selectively adheres to narrow regions between the structure and the wall of the chamber. *Stentor* causes flow by using membranelles around the cell "mouth" for feeding. I found that most cells direct the cell mouth to broad areas at narrow regions.

Selecting behaviours of anchoring location affected by geometrical cues

I observed the anchoring behaviours in geometrical chambers consisting of several narrow areas. From these observations, *Stentor* cells select anchoring locations affected by geometrical cues such as angle and curvature forming these corners. The swimming cells are often found along the wall of the chamber and in narrow areas. On the other hand, the cell selects its anchoring location to a smaller angle and shaper corners.

I observed the swimming behaviours in each narrow area to understand the mechanism of selecting the anchoring location in the *Stentor*. When the cell encounters narrow regions, the cell takes two types of escaping behaviour. In the smooth corner, the cell escapes by swimming along the wall. On the other hand, in the sharp corner, they repeat backwards swimming accompanied by ciliary reversal. Quantification of the behaviour reveals that reversal of swimming direction frequently occurs in narrow regions significantly compared with wide regions. It indicates that frequent ciliary reversal by collision at the narrow area affects the behavioural transition from swimming to adhering.

Discussion

In previous, Théry reported that *Stentor*'s feed *Chlamydomonas* accumulate corner. In addition, *Stentor* performs avoiding response as quick contraction when their predators come into contact with the cell. So, when the cell attaches to narrower regions, it can hide from predators and wait for prey. In drying conditions, water accumulates in narrow regions. So, *Stentor* attaching narrow areas may live longer.

In this study, the behavioural transitions of the ciliate of *S. coeruleus* were described for the first time using quantitative analysis. We found that the anchoring behaviour of trumpet-shaped cell is selective in confined spaces and that the geometric structure of the outer space influences the transition of cell states.

From this thesis, I showed that the behavioural transitions of unicellular organisms interact with the physical factor of geometry. It is the first study to investigate the relationship between extracellular geometry in their habitats and behavioural transitions. These methods in this thesis will help approach the survival strategies of many uncharacterised species of microorganisms.

2 Introduction

Protists are eukaryotic cells, almost unicellular organisms, except for animals, plants and fungi. They are ubiquitously in nature and have many varieties of shape and motility. They have survived in complex habitats for hundreds of millions of years. This thesis focuses on a living strategy in swimming ciliate *Stentor coeruleus*, a 1 mm long trumpet-shaped blue single-cell. In this section, I introduce the background of protists' behaviour, focusing on the variety of motility in microorganisms, especially *Stentor*. I also added to the connection between microscale motility and physics, such as hydrodynamics. Based on these backgrounds, I introduce a research question in this thesis.

2.1 About Protist

Protists are eukaryotic cells, not including animal, plant and fungi. Recently, molecular biological analysis revealed the protist's diversity, and then its classification was revised, and another eukaryote classification system was suggested (Adl et al., 2005, 2012, 2019). Eukaryotes are classified into groups named supergroups based on the genome analysis, not on morphology like a five-kingdom classification. The classification revealed that the protists previously classified have a large variety in eukaryotes compared to animals and plants. The previous classification had a bias from humanity.

Protists account for a large portion of eukaryotes, are almost unicellular, and the size of the cell is barely visible to the naked eye. The structure of the protists is simple compared to multicellular organisms one. However, these protists have survived over 1 billion years (Dacks et al., 2016; Hedges et al., 2004; Eme et al., 2014) and some protist fossil have been found in Cretaceous amber in their present forms (Martín-González et al., 2008). It has considered that these protists have survived in harsh environments for geological time. During this period, there have been environmental changes and mass extinction. To survive these environments, diversity of organelles structures (Müller Miklós et al., 2012), excitabilities (Wan and Jékely, 2021) and motilities (Bondoc-Naumovitz et al., 2023) in the eukaryotic cells may contribute to their livings.

2.1.1 Many variety of motility in protists

In this thesis, I focus on the behaviour of a ciliate, and I will explain the variety of the motilities in microorganisms out of this diversity. Motilities in microorganisms are mainly divided into swimming and surface motility (Bondoc-Naumovitz et al., 2023). *Paramecium* or bacteria (not protists) have cilia or flagella, rod-like structures causing flow for swimming. On a substrate, one of the ciliate, *Euplotes*, has another motility that behaves like walking on a substrate using ciliary bundles named "cirri", like our legs (Larson et al., 2022). In addition, *Amoeba* crows for locomotion and feeding using pseudopodia. Diatom and some ciliates also crow. *Chlamydomonas* has two

motilities: the cell swims in water or the cell glides on a surface by its flagellar adhering to the substrate (Lewin, 1952; Bloodgood, 1981).

The classification of the motility is made by simplifying their motility. In the natural behaviours of the cell, these cells perform their complex behaviours rather than previously explained ones. These complex behaviours of the cells have been reported from one hundred years ago (Jennings, 1906). It reported that a ciliate, *Stentor*, takes avoiding response with the order of hieratical reaction responding to the same repeated stimulus (Jennings, 1902; Dexter et al., 2019; Trinh et al., 2019), and *A. proteus* binds a *Spirogyra* in the cell (Jennings, 1906). Many of these behaviours have been reported, but most of the reports are descriptive. The biological mechanism of these behaviours has not been understood, and quantitative analysis of these cells is not too much.

2.1.2 the importance of quantification about microorganism behaviour

The sizes of these protists are small compared to the scale we can recognize. However, they play roles in macroscopic environmental issues such as substance circulation (Sanders and Wickham, 1993; Lynn, 2008), water purification (Fenchel, 1982), and red tide (Sellner et al., 2003). These phenomena consist of each cell's motilities, and quantitative analysis of behaviours is essential for understanding the issues.

In addition to revealing the environmental phenomena, quantifying these behaviours is an important approach to understanding their strategies. These unicellular organisms live in complex environments; there are unpredictable time-varying surrounding environments such as temperature, light, and concentration of chemical components, and there are heterogeneous distributions of their prey and predator (Barry and Dayton, 1991). In these habitats, what information the cell obtains and, from this information, how the cell reacts and what behaviour performs is a mystery. Quantification of the behaviours provides the connection of the behaviour and strategy that has been left for a long time and understanding of the living systems in simple unicellular organisms.

Next, I will introduce ciliated protozoa, *Stentor*, that recently shed light on unicellular learning. In this thesis, I report the behavioural transition in *Stentor*, in which the cell changes its motility, accompanying the cell shape, using geometrical cues around it. Indeed, one behavioural transition from swimming to anchoring, selecting an anchoring location, is focused.

2.2 *Stentor* and several behavioural responses

2.2.1 Behaviour of *Stentor*

Stentor is a large single-celled organism (0.5–1 mm) belonging to the phylum Ciliophora in the order Heterotrichida (Adl et al., 2019) (Figure 2-1). This organism has been well studied for wound healing and regeneration (Tartar, 1961; Blauch et al., 2017; Marshall, 2021) because it is not hard for microsurgery of large cells. From microsurgery, several complex regeneration processes have been well studied (Tartar, 1961). The axis of anterior and posterior served in intracellular. The

whole genome has been read (Slabodnick et al., 2017), and these mechanisms have been studied from molecular biology. Using microfluidic devices, the efficiency of successive regeneration probability rises compared with manual microsurgery by hand (Blauch et al., 2017; Zhang et al., 2021). So, the mechanism of the regeneration process will be revealed from molecularly.

On the other hand, other research has been reported about their ecology and behaviours. The entire body surface of the *Stentor* is covered in cilia for swimming by generating flow. On the edge of the oral region (peristome), the cilia are also tightly packed (membranelle), i.e., two or three rows of cilia (20–25 cilia in each row) (Randall and Jackson, 1958). The membranelles are components of a ring-like oral structure (membranellar band). The membranelles collectively beat, and each membranelle beat slightly later than the next as a metachronal wave. The membranelles stir the fluid to generate a feeding vortex (Maupas, 1888), which brings food to the oral apparatus. When the cells form a colony, they cooperatively stir the fluid, and the feeding velocity is raised hydrodynamically (Shekhar et al., 2023).

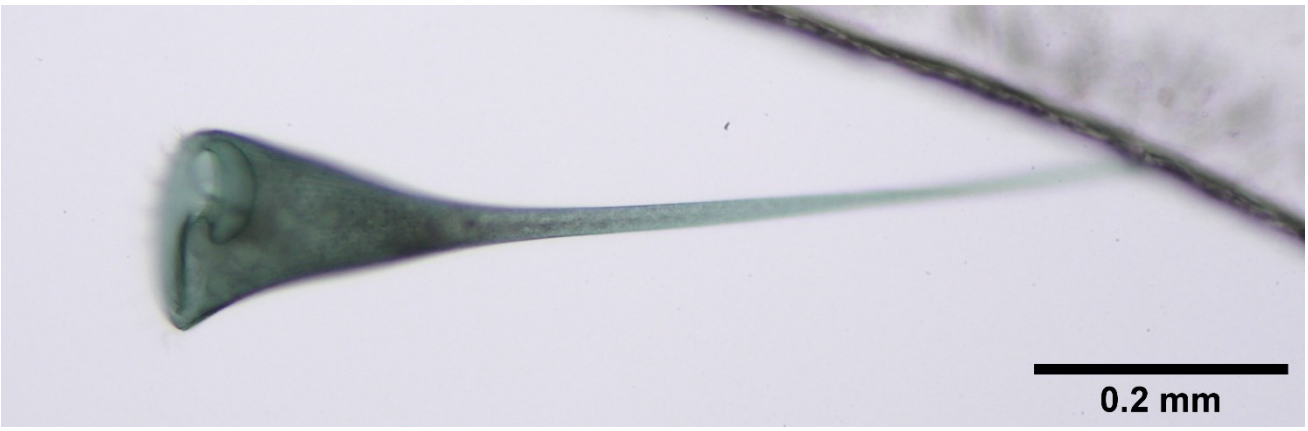

Figure 2-1 Adhering *S. coeruleus*.

1 mm long blue-green ciliated protozoa, *S. coeruleus* has mainly two motilities, swimming and adhering. The posterior region of the cell (sharp region, right-hand side) attaches to a substrate. Ciliary bands, membranelles around the cell "mouth" in the anterior region (left-hand side) cause flow for feeding.

Although *Stentor* exhibit free swimming, they become sessile once attached to the structures. We can see *Stentor* adhering to dead leaves, twig duckweed, *Spirogyra* mats and dead cattail leaves (Tartar, 1961). Switching its motility may depend on the intra- and extracellular conditions. Light affects their behaviours; that is, a negative photoresponse can be caused by the coloured pigment Stentorin under the near cell surface (Song et al., 1980b; a; Iwatsuki, 1992). Its photoresponses are caused by ciliary beating regulated intracellular conditions such as membrane potential and the

concentration of Ca ion (Iwatsuki and Song, 1989; Song, 1999). In addition to the photoresponse, avoiding reaction is also known as regulating the Ca concentration (Huang and Pitelka, 1973). Recently, Dexter et al. reported that "complex decision-making" in *Stentor* (Dexter et al., 2019) relates to intracellular conditions (Trinh et al., 2019). In the following sections, I explain a ciliary reversal in photoresponse and a quick contraction as avoiding response triggered mechanical stimuli. Those behavioural changes have been well studied from the relationship between intracellular states and behaviours.

2.2.2 Photoresponse

Photoresponses in *S. coeruleus* have been well studied. These three reactions contribute to accumulation in a dark field. The swimming speed of the cell depends on the light intensity (Photokinesis) (Iwatsuki, 1992). When the cell encounters the difference in light intensity from a dark to a bright area, it behaves the ciliary reversal and turns its swimming direction (step-up photophobic response) (Song et al., 1980a). Once the cell swims to the light source, it also behaves in ciliary reversal and turns to the opposite side of the light (negative phototaxis) (Song et al., 1980b). These two reactions, photophobic response and phototaxis, are accompanied by ciliary reversal, and these action spectrums are very similar (Wood, 1976).

S. coeruleus is a blue-green coloured organism. Blue granules are embedded on the cell surface (Inaba, 1959); we can see the vertical stripe pattern on the cell. The absorption spectrums of this pigment are similar to the action spectrum in living *S. coeruleus* and the absorption spectrum in crushed cells (Walker et al., 1979). These results show that the blue pigments have been considered a photoreceptor in the cell. However, its chemical structure and properties differ from rhodopsin, a mammalian photoreceptor (Tao et al., 1993). There are two types of Stentorin, Stentorin I and II (Moller, 1962). Moreover, Stentorin II contributes to photoreceptor protein because of its pre-photoresponse property (Savikhin et al., 1993; Song et al., 1990).

The motility of photoresponses (step-up photophobic response and negative phototaxis) are caused by ciliary reversal, which is regulated by intracellular condition such as membrane potential or concentration change of Ca ion (Song, 1981). Light absorption changes the structure of Stentorin II, and the component releases a proton. Then, the decrease of intracellular pH occurs, which induces an influx of Ca. Finally, it caused ciliary reversal. The concentration of ion components contributes to membrane potential.

These intracellular conditions regulate the behavioural activity of ciliates, such as a very quick contraction as avoiding reaction in *S. coeruleus*, which is also well studied from the intracellular mechanism and cellular learning. The following section will discuss cell deformation and the relationship between a mechanical stimulus and a behavioural transition accompanying cell deformation.

2.2.3 Cell deformation and behavioral changes in *S. coeruleus*

Stentor mainly exhibits three shape states: a droplet, a cone and a trumpet (Tartar, 1961). The cilia covering the cell surface cause flow for swimming. In free swimming, the cell forms a cone shape. On the other hand, trumpet-shaped cells slowly swim or attach to substances for feeding. This behavioural transition from swimming to adhering accompanies cell deformation. During the adherence process, *Stentor* anchors to a surface using an adherent structure (holdfast) at the posterior end, where mucus is secreted (Andrews, 1945). Previously, the holdfast had been considered a suction for adhering organs (Gruber, 1878), but the cilia at the holdfast attach to a substrate (Andrews, 1945). Mechanical stimuli and light produce a quick contraction from cone or trumpet shapes to droplet shapes as avoidance behaviour (Wood, 1969). The cell habituates its mechanical stimuli, and the behaviour has been studied from electrophysiology (Wood, 1970, 1988). Its contraction depends on Ca ion binding protein myoneme independent ATP (Wood, 1982; Huang and Pitelka, 1973). The molecular structure of the myoneme has not been revealed clearly. In *Spirostomum*, many people are trying some mechanism of quick contractions and phylogenetic analysis of myoneme (Chang and Prakash, 2023; Zhang et al., 2023). One behavioural transition from trumpet to droplet as avoiding reaction is caused by intracellular property triggered mechanical stimuli. The next section explains the relationship between behavioural change and mechanical stimuli.

2.2.4 Quick contraction triggered by mechanical stimulus

The quick contraction from trumpet to droplet has been well studied. The mechanoreceptor channel on the cell surface reacts to the mechanical stimulus, triggering its behavioural change (Wood, 1989). Through this channel, it induces the Ca ion influx and membrane potential increases. Once the potential exceeds some threshold, the quick contraction occurs, and the potential also bursts and returns to resting potential (Wood, 1988). The duration time from mechanical stimuli to initial reaction is several ms order (Newman, 1972). The contraction is also ms order; the half contraction takes several ms (Wood, 1970).

When we repeatedly induce the quick contraction, it is not easy to contract (habituation); it is a primitive learning ability (Wood, 1969, 1988). So, the cell has been studied from cellular learning. Recently, Rajan et al. reported that the cell switches from a non-habituated to habituated state by statical analysis of the sequence of single-cell behaviours (Rajan et al., 2023). The hierarchical avoidance response previously reported by Jennings (Jennings, 1902) has been reproduced (Dexter et al., 2019), and machine learning does not predict these complex behaviours (Trinh et al., 2019). From these results, *Stentor* has the capacity to react to a variety of stimuli, and they may exhibit suitable behavioural transitions.

2.3 Research question

Behavioural transitions in *Stentor* occur in complex environments. The surrounding environment of the cell varies every moment, and the adhering cell will go away when the cell receives some unsuitable stimulus (Jennings, 1906). The location that the cell initially anchors also varies with the situation. So, the cell must perform behavioural change properly. Then how does the cell select the anchoring location in the behavioural change from swimming to adhering? Does the cell randomly attach or not? When we collect pond water in nature, we sometimes find that *Stentor* cells anchor to complex geometrical micro-sediments in their habitats.

2.3.1 Micro-sediments and its shape

In nature, there are ubiquitous micro-sediments with many shapes, such as twigs, dead leaves and dead bodies. These structures have a micro-complex geometrical shape. When we collect pond water, we sometimes see the anchoring *Stentor* on the surface of micro sediments (Figure 2-2).

The behaviour of ciliates is affected by a substrate or geometry surrounding the cell caused by hydrodynamical interactions. For example, the ciliate, *Tetrahymena*, slides on a substrate by hydrodynamical interaction between the surface velocity and a substrate, and the cell shape also causes this behaviour (Ohmura et al., 2018). Furthermore, the ciliates perform a swim upstream caused by hydrodynamical interaction between the external flow and the flow caused by the ciliate (Ohmura et al., 2021). In addition, the ciliates can escape from a dead end formed by flat two plates hydrodynamically (Ishikawa and Kikuchi, 2018). When this cell, such as *Tetrahymena* or *Paramecium*, encounters a dead end or confinements, the cell escapes by more extended ciliary reversal (Kunita et al., 2014) or the swimming trajectory is changed to the size of the previous arena by intracellular mechanisms such as membrane potential change or Ca ion influx (Kunita et al., 2016). These ciliates control the beating form of cilia, and it causes their swimming trajectory. When the cells collide with a pillar from its front, they react in ciliary reversal and turn the direction; on the other hand, when the cells collide from an angle or its side, they do not change their ciliary beating (Naitoh and Eckert, 1969) and go away hydrodynamical interaction to a pillar (Escoubet et al., 2023).

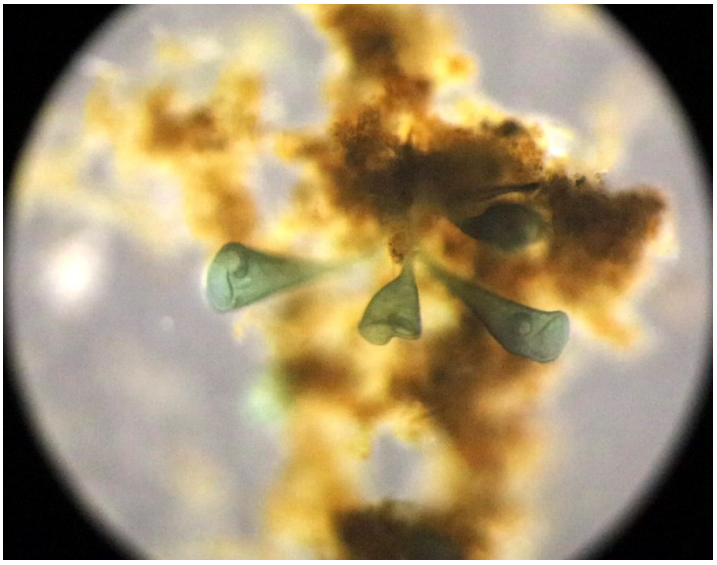

Figure 2-2 Anchoring cell to micro geometrical sediments in nature.

Three elongate cells attach to a structure. Posterior regions of each cell adhere to groove of the sediment.

2.3.2 The influences of geometrical structure to their strategies

From these results, extracellular geometry and geometrical shape hydrodynamically affect ciliates' behaviour (Théry et al., 2021; Escoubet et al., 2023). Filter feeders like *Stentor* and *Vorticella* cause flow around the cells and capture the prey in their mouth using the flow. So, the structure of the feeding flow is affected by surrounding geometry and must influence the feeding efficiency (Pepper et al., 2010, 2013). In addition, there are environmental changes such as external flow or drying conditions. Therefore, anchoring the location of the *Stentor* is essential for their living.

However, the behavioral transition from swimming to adhering has not been focused (Andrews, 1945). In this study, I will focus on the influences of geometrical micro-structure around the cell for selecting anchoring locations. I aim to reveal the mechanisms of spatial sensing: what external cues induce the behavioural change from swimming to adhering. So, I quantitatively evaluated the effect of extracellular structures on the *Stentor*'s behaviour.

3 Methods

In this part, I described experimental procedures and behavioural analysis. I conducted four types of experiments. First, I observed the cell behaviour in a simple chamber. Second, I made the observation chamber with/without a structure; thirdly, I changed the structure parametrically and measured the anchoring selection behaviour. Finally, we experimented to understand the mechanism of anchoring to a narrow area and the trigger of behavioural change. These methods are basically described in Echigoya et al., 2022 (Echigoya et al., 2022).

3.1 Cell cultures

In observing experiment in simple chamber, *S. coeruleus* was collected from the pond at Tomakomai located Hokkaido, Japan (42.67°N, 141.59°W) and was maintained in a 96-well cell culture plate (TR5003, TrueLine, United States; 6.4 mm diameter) containing filtered pond water using a Millex 0.22 µm filter (Merck Millipore, Burlington, MA, United States) at room temperature in the dark. We placed *Cryptomonas paramecium* into the culture plate as the *Stentor*'s feed, which was axenically grown in a CHM medium (0.1% $CH_3COONa \cdot 3H_2O$, 0.1% "Lab-Lemco" powder (Oxoid L29) in Milli-Q water; adjusted pH 6.9 ± 0.1 with 1 N NaOH) under light-dark conditions (12 h:12 h) at room temperature every three or 4 days. We transferred *C. paramecium* to a fresh CHM medium every week.

In the experiments using chambers with/without structure, cells were collected from the Shiribetsu River located in Hokkaido, Japan (42.81°N, 140.69°W) and cultured at 25°C in a 6 cm diameter plastic dish containing modified Peters' solution (0.55 mM $CaCl_2$, 0.15 mM $MgSO_4$, 0.15 mM K_2CO_3 and 0.75 mM Na_2CO_3, adjusted pH 7.4 ± 0.1 with 1 N HCl) in the dark (de Terra, 1966) with one wheat grain (MRP-706, Marukan, Osaka, Japan). The cells were transferred into a fresh medium to maintain the cultures every 2–3 weeks. The difference in the strain was not significant in our experiment (detailed in Figure 3-1).

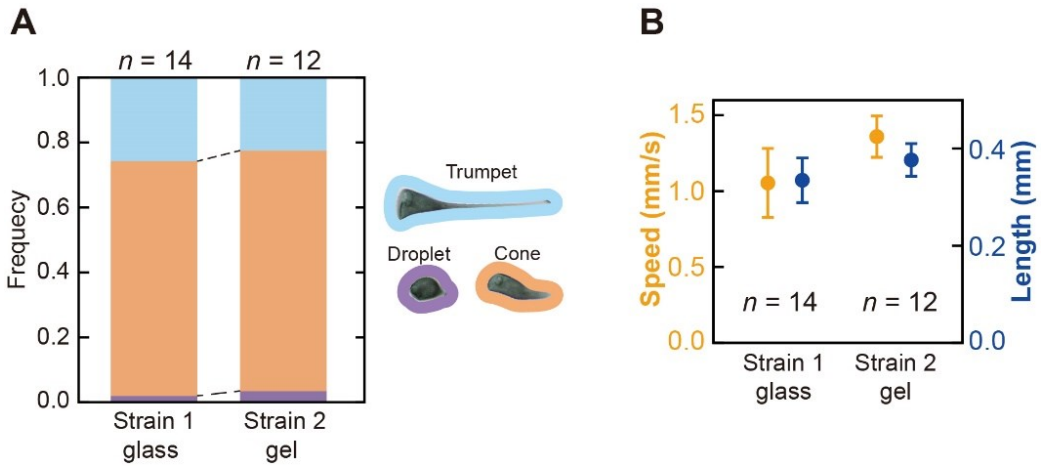

Figure 3-1 The differences between the 2 strains.

(A)The frequencies of the cell states. The difference in the strain was not significant in our experiment. Cone-, trumpet- and droplet-shaped cells were observed in 72.3%, 25.7% and 2.0%, respectively in strain 1 (obtained from Tomakomai) in a glass chamber; In strain 2 (obtained from Shiribetsu River) in the gel chamber, cone-, trumpet- and droplet-shaped cells were observed in 74.1%, 22.4% and 3.5%.
(B) In strain 1 (obtained from Tomakomai) in a glass chamber, the speed and length were 1.05 ± 0.23 mm/s and 0.33 ± 0.046 mm (SD, n = 14), respectively. In strain 2 (obtained from Shiribetsu River) in the gel chamber, the speed and length are 1.35 ± 0.14 mm/s and 0.38 ± 0.034 mm (SD, n = 12), respectively.
*Created by modifying (Echigoya et al., 2022) (© 2022 Echigoya, Sato, Kishida, Nakagaki and Nishigami (Licensed under CC BY 4.0)) https://creativecommons.org/licenses/by/4.0/

3.2 Observation method

Before the observations, we washed the cells in fresh pond water twice in order to eliminate chemical effects and starved them for 3 days. Prior to transferring a cell into an observation chamber, we washed the cell with fresh pond water again and equilibrated it for over 20 min (Figure 3-2A). The observation chamber was made of a silicon sheet (244-6012-03, HAGITEC Co., Ltd., Chiba, Japan; 0.2 mm depth, 5 mm inner diameter) and covered by a cover slip (Figure 3-2B). Cell behavior was observed by an inverted microscope IX73 (Olympus, Tokyo, Japan) equipped with a PLANPO X1.25 objective (Olympus, Tokyo, Japan). Images were recorded by using a CMOS camera (ORCA-Flash4.0 v2, Hamamatsu Photonics, Hamamatsu, Japan) with an exposure time of 5.0 ms and a frame rate of 10 frames per second (fps) under a brightness field using weak 700 nm light (M700L4, Thorlabs, New Jersey, United States) to reduce the photoresponse effects (Song et al., 1980b; a; Iwatsuki, 1992).

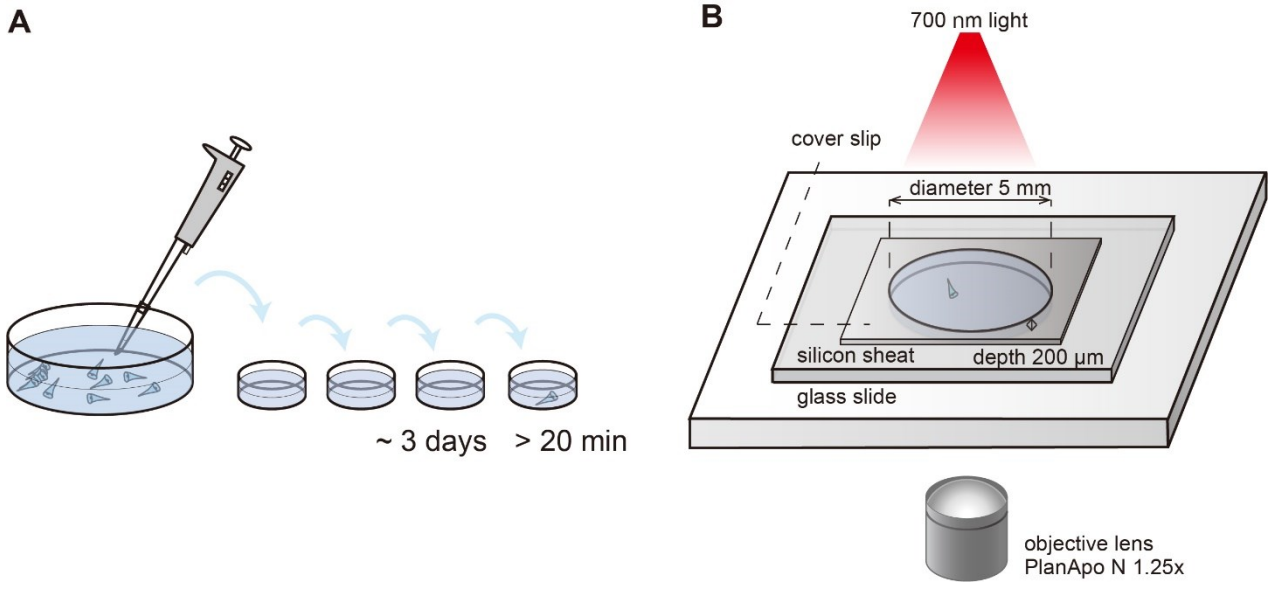

Figure 3-2 Experimental setups.

(A) Washing cells. (B) Observation method.
*Created by modifying (Echigoya et al., 2022) (© 2022 Echigoya, Sato, Kishida, Nakagaki and Nishigami (Licensed under CC BY 4.0)) https://creativecommons.org/licenses/by/4.0/

We used 14 cells for measuring the swimming speed and the cell length over 25 min after placing them in the chamber (24.7 ± 3.4 min (SD, 14 cells, maximum 32.0 min, minimum 18.6 min, total 345.1 min: All behavioural data are shown in Figure 3-3). To measure the duration time of each shape transition and the diameter of the swimming trajectory in the trumpet shape, we additionally recorded the cell behaviors and analyzed the data (Figure 3-4). Because of the very low frequency at the droplet state, we obtained the behaviors of the cells in the droplet state by adding an external mechanical stimulus to calculate a transition vector and conducted computational classification of the cell state (Figure 3-4).

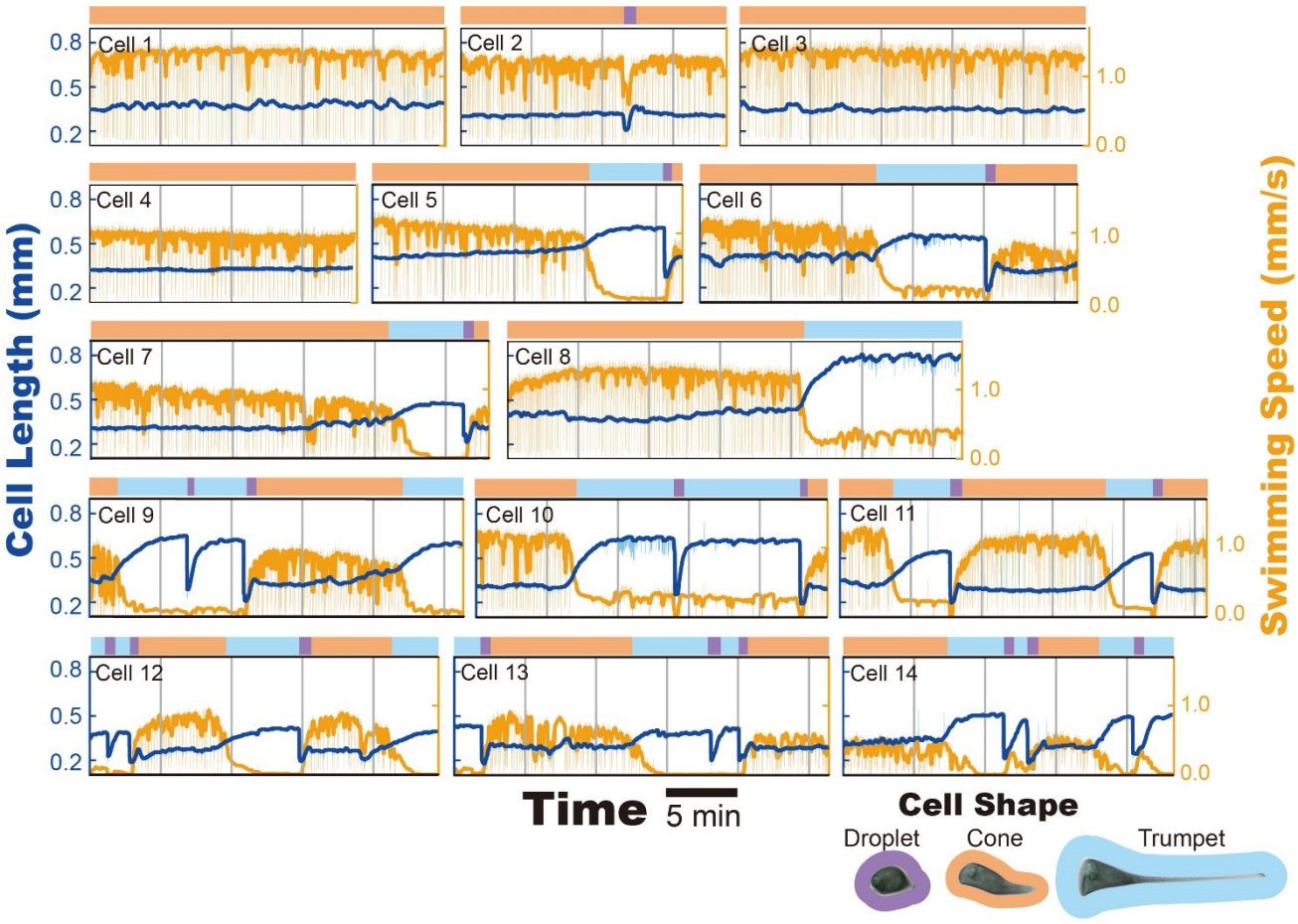

Figure 3-3 The time series of the cell length (blue line) and swimming speed (orange line) in 14 cells.

We used 14 cells to obtain the frequencies of each cell state. Recording time in each cell is 24.7 ± 3.4 min (SD, 14 cells, maximum 32.0 min, minimum 18.6 min, total 345.1 min). Cells 1–4 take the steady cone state, others change their states frequently (Cells 9–14). There is a variation in the frequency of changing the states among those cells (Cells 5–8).
*Created by modifying (Echigoya et al., 2022) (© 2022 Echigoya, Sato, Kishida, Nakagaki and Nishigami (Licensed under CC BY 4.0)) https://creativecommons.org/licenses/by/4.0/

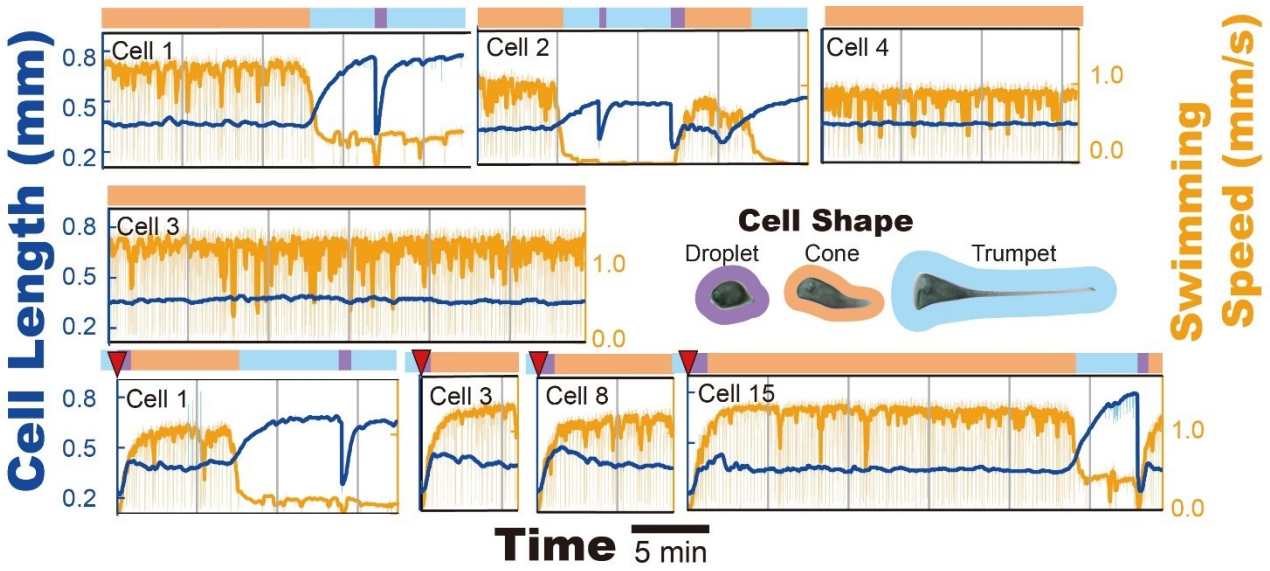

Figure 3-4 Additional data for quantitative measurements of cell behavior.

To measure the duration time of each shape transition and the diameter of the swimming trajectory in the trumpet shape, we additionally recorded the cell behaviors and analyzed the data. Red rectangle symbol means an external mechanical stimulus.
*Created by modifying (Echigoya et al., 2022) (© 2022 Echigoya, Sato, Kishida, Nakagaki and Nishigami (Licensed under CC BY 4.0)) https://creativecommons.org/licenses/by/4.0/

Due to very quick contraction from the trumpet to the droplet shape, we recorded the contractions of eight cells by the high-speed camera FASTCAM Mini AX50 (Photron, Tokyo, Japan) at 2,000 fps and an exposure time of 1/2,000 s. Images were collected by using the IX73 microscope with a UNLPlan X10 (Olympus, Tokyo, Japan) objective under 700 nm light.

When we observed the shape transitions from the trumpet shape to the droplet shape, we added an external stimulus by striking the chamber using a tweezer.

Prior to observing anchoringbehaviours in the chamber with/without an obstacle, cells were washed twice in a fresh medium and starved for several hours. The gel chambers were then placed on a cover slip, and their surfaces were wetted with medium before being covered with a plasma-coated glass slip for 20 s. After that, a glass slide on the chamber was slid until a swimming arena appeared, and the cell was transferred into the chamber from the edge of the glass slide using a pipette tip. The inner surface of the tip was coated with the 2% 2-methacryloyloxyethyl phosphorylcholine (MPC) polymer Lipidure® CM5206 (NOF Corporation, Tokyo, Japan) in ethanol (weight per volume) to prevent cell adhesion. uring this process, most cells quickly contracted in response to external stimuli; however, the cell swam after several seconds. Finally, we slowly slid the cover slip to cover the observation chamber.

The behaviors were observed by using a SZX16 stereomicroscope (Olympus, Tokyo, Japan) equipped with a C-Mount Adaptor 0.5X, U-TV0.5XC-3 (Olympus, Tokyo, Japan) and a CMOS camera, ORCA-spark C11440-36U (Hamamatsu Photonics, Hamamatsu, Japan). The exposure time was set to 50 ms at 4 fps. A 2 × 2 binning scheme was employed under dim white light, filtered through a red pass plate, for approximately 40 minutes. The quantum sensor MQ-610 (Apogee Instruments, Utah, United States) could not detect the observation light due to weakness [<1 μmol s^{-1} m^{-2} ~ 0.2 W/m^2 (650 nm)]. Less than 0.2 W/m^2 red light has little influence on the phototactic behavior (Song et al., 1980b).

In the experiments involving the selection of locations in geometrical chambers, we observed the one-cell behaviour using a stereomicroscope SZX16 equipped with a 2.5X objective lens, under a red-filtered brightness field positioned 5 mm above the stage. The behaviour was recorded by a CMOS camera connected by 0.5X converter for about 40 minutes, with settings of 50 ms exposure, 4 fp, and 2x2 binning for prevent the effect of photoresponses in *S. coeruleus*.

Subsequently, we manually aligned the orientation and position of the chamber in each recording using a background image calculated by the median intensity at each pixel over time, specifically for manually selected swimming periods. The images, which calculated intensity differences between sequential images and the background image, were conducted Gaussian blur (radius 1 pixel), and were converted to binary images using MaxEntropy method (Kapur et al., 1985). Finally, we derive a time series of the centres of the cell from the contours. Anchoring positions and anchoring duration times were manually determined.

3.3 Quantification of cell length and swimming speed

To quantify cell behaviors, the following image analysis was conducted. First, we analyzed the data containing no external stimulus. We cutoff sequential images to several sections (2,000–5,000 frames) and obtained each background image by calculating the local median intensity. Then, the background-subtracted sequential images were subjected to Gaussian blurring (radius = 1.1 pixels), and binary images were acquired using the MaxEntropy threshold algorithm (Kapur et al., 1985). After that, we obtained the centers C_i: $\boldsymbol{r}_i = (x_i, y_i)$ (mm) of the cells at the i th frame. To measure the cell length, we obtained the length l_i (θ) from the center of the cell to the edge by converting images to polar coordinates in 2° increments (Figure 3-5). The cell length L_i was defined by $L_i = l_i(\theta_1) + l_i(\theta_2)$, where $l_i(\theta_1)$ and $l_i(\theta_2)$ represent the top two local maxima of $l_i(\theta)$, and θ_1 and θ_2 indicate the directions of the anterior and posterior directions, respectively (Figure 3-5).

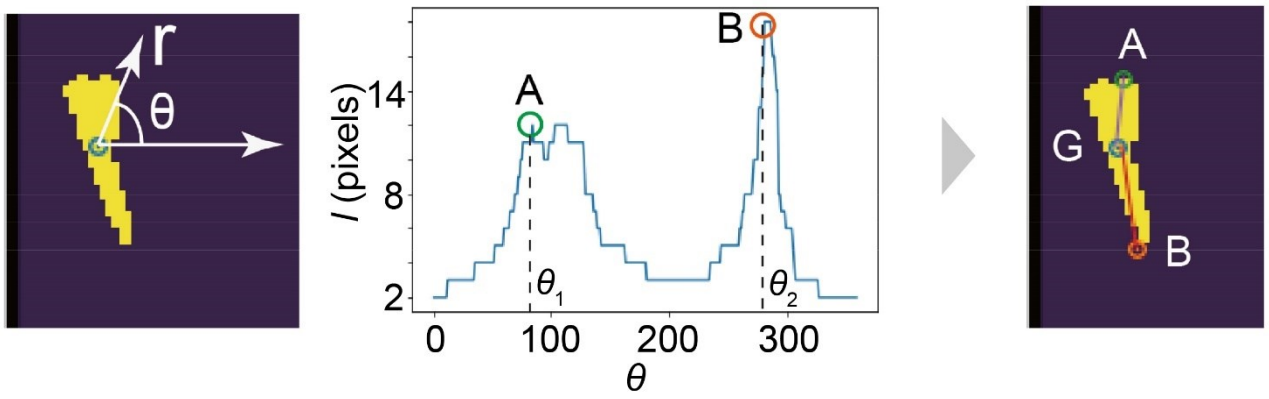

Figure 3-5 The methods of obtaining the length of the cell.

We measured the distance from the centre (G) to the contour of the cell with respect to the angle, theta (left figure and middle figure). The top two local maximums (A and B in middle figure) were selected, and the cell length was defined by the sum of the two lengths AG + BG (right figure).
*Created by modifying (Echigoya et al., 2022) (© 2022 Echigoya, Sato, Kishida, Nakagaki and Nishigami (Licensed under CC BY 4.0)) https://creativecommons.org/licenses/by/4.0/

Instantaneous swimming speeds $s_i = |\boldsymbol{v}_i|$ were calculated from the center of the cell C_i, defined by $\boldsymbol{v}_i = 0.5\,[(\boldsymbol{r}_{i+1} - \boldsymbol{r}_{i-1}) \cdot \mathrm{fps}]$ (mm/s). Because of the difficulties of determining the shape and center of the cell caused by its thin posterior region and fusion with air bubbles, we obtained a smoothed time series of the cell length L'_i and speed s'_i from the median values for ± 5 s (50 frames) for an overview of behaviours; ± 3 s (30 frames) for measuring the time duration from cone to trumpet; and ± 1 s (10 frames) for measuring the time duration from droplet to cone and from droplet to trumpet.

During the contraction process from trumpet to droplet induced by an external mechanical stimulus, we manually identified three points: the posterior end (P) and two edges of the oral apparatus, OA_1 and OA_2. Then, we calculated the middle point (M) between OA_1 and OA_2, and the cell length L was determined as the distance between M and P.

The procedure for determining the cell locations in geometrical chambers followed a similar approach. Whenever an error occurred, we adjusted a parameter or changed the order of image processing.

3.4 The estimation of the frequencies of each cell state

For an overview of behaviors and comparison with the computational classification of the cell states (see Section 3.5), we divided the behaviors into three states (droplet, cone and trumpet) based on Tartar's descriptive classification (Tartar, 1961). Then, we obtained the frequency of the cell states

and the distributions of the cell length and swimming speed at each state. Normalized length $\tilde{L}$ and speed $\tilde{s}$ were calculated b averaging length L_0 and speed s_0 in each free-swimming cell in the cone state for 10 s (the parameters were the same in all experiments). The normalized values at the i th frame were defined by

$\tilde{L}_i = L'_i/L_0$, $\tilde{s}_i = s'_i/s_0$,

where L'_i and s'_i were the median values for ± 5 s (the parameter was the same in all experiments) with respect to the length L and speed s, respectively. In one sample from the gel chamber with a structure, the average length and speed were determined as $L_0 = 0.5$ and $s_0 = 0.9$ because most of the state in this cell was adhesion, and we could not extract averaged values at the swimming state. The bin width was 0.03 (normalized).

3.5 The computational classification of cellular states in the state field

We excluded the transition periods (±15 s of droplet state, ±60 s of cone state, ±30 s of trumpet state) to classify the steady states of the cells computationally. Hierarchical cluster analysis was performed to divide the cell states into three clusters using the "AgglomerativeClustering" function from the "sklearn.cluster" library in Python (Pedregosa et al., 2011). The parameters used in the clustering method were the number of clusters ("nclusters"): 3, "affinity": Euclidean, "linkage": complete. Due to computational memory limitations, downsampling was applied to the data points (±5 s median values) using a 10-increment sampling method.

3.6 Fabrication techniques and observation methods in geometrical chamber

In the experiment using chamber with/without structure, the observation chambers were made by mold casting in two processes: preparing prime molds using polydimethylsiloxane (PDMS) and forming gel chambers by pouring agarose gel into the PDMS molds. We made two types of chambers. One is the chamber (diameter 5 mm, depth 0.3 mm) with a disk-like structure (diameter 2.5 mm), and the another is the chamber (diameter 5 mm, depth 0.3 mm) without any structure (Figure 3-6).

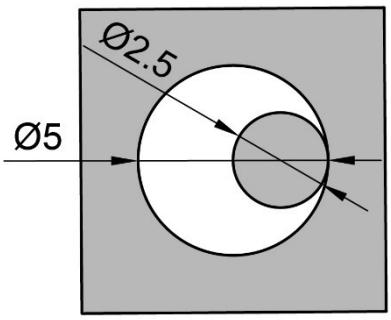

Figure 3-6 Geometry of the chamber with a structure.

*Created by modifying (Echigoya et al., 2022) (© 2022 Echigoya, Sato, Kishida, Nakagaki and Nishigami (Licensed under CC BY 4.0)) https://creativecommons.org/licenses/by/4.0/

The prime mold data were designed using Fusion 360 software (Autodesk, California, United States). These data were sent to a CAMM-3 Model PNC-3200 milling machine (Roland DG Corporation, Hamamatsu, Japan) using MODELA Player Version 3.7 (Roland DG Corporation, Hamamatsu, Japan), and prime molds were made by cutting with a ZW-100 (Roland DG Corporation, Hamamatsu, Japan). The cutting process involved three steps: surface cutting, rough cutting and finish cutting. Each cutting parameter were selected suitably. For rough cutting and finish cutting of the chamber with structure, we used the micro end mill, MHRH230 φ0.2 × 2 (NS TOOL, Tokyo, Japan). In other processes, the end mill 2CEM-G-2.5D-2 (MonotaRO, Hyogo, Japan) was used.

PDMS was prepared by mixing the prepolymer and the curing agent of the SYLGARD™184 silicone elastomer kit (Dow Corporate, Michigan, United States) in a 10:1 (weight: weight) ratio. The mixture was mixed for 20–30 min and then vacuum-degassed for approximately 1 h. The degassed mixture was poured into moulds and vacuum-degassed again for approximately 1 h. The PDMS prime chambers, covering a glass slide were kept horizontally at 25°C. After 48 h, the PDMS prime chambers were removed from the moulds.

Prior to obtaining the observation chambers, the surface of the PDMS chamber underwent a cleaning process involving washing with ethanol and Milli-Q water, followed by sonication in reverse osmosis water. These processes were repeated three times or more. Then, the surface was rinsed with Milli-Q water and dried. Plasma coating (PC-400T, STREX, Osaka, Japan) was then applied for 10–20 s to hydrophilize the surface.

A mixture of the 2% (weight per volume) agarose (PrimeGel™ Agarose LE 1–20K, Takara Bio, Shiga, Japan) medium that melted in the fresh modified Peters' solution was poured into PDMS molds and covered with a cover slip to flatten the agar chambers. After 2–3 min, the cover slip was vertically removed, and the agar chambers were extracted from the PDMS prime mold. If we could

not remove the agar chambers by the above methods, then the chamber was removed by sonication using the ultrasonic cleaner US-5KS (SND, Nagano, Japan) containing reverse osmosis water.

In the geometrical chambers, these chambers were also made by 2% agarose gel (PrmeGel) using wax molds. For preparation these molds, we designed three-dimensional data using a 3DCAD software, Fusion360 (Autodesk, California, United States) and sent the data to CAMM-3 Model PNC-3200 milling machine via MODELA Player Version 3.7 (Roland DG Corporation, Hamamatsu, Japan). There are three cutting processes: planer cutting, rough cutting, and precise cutting. A mold was cut by an extra-fine endmill based on the 3D data. The type of mill and cutting parameters in each chamber are properly selected.

Prior to the observations, we prepared the observation agarose chambers. We mixed the 2% agarose gel (weight/volume) and filled it with fresh Modified Peter's solution to melt the agarose gel. Then, the mixture was gently heated using a magnetic hot stirrer (RCH-1000, Eyela, 110 °C; 80–100 rpm) in a conical flask (25 mL, corning) covered by plastic wrap to prevent evaporation. After one to several hours, the mixture became transparent, and we transferred the melting gel to the mould by pipet to prevent air bubbles. A mould filled with agarose gel was filled with a glass slide to flatten the bottom of the gel chamber. We melted agarose sets several minutes later, took them out from a mould using a spatula, and immersed the gel chambers in a fresh medium. These chambers were used within several hours. There are some exceptions in making the star chamber, such as using a 300 W microwave to melt the agarose and a hotplate to maintain the melting state.

We put one gel chamber on a glass slide and rinse the surface of the chamber by the medium once. Then, we filled the observation chamber with medium and covered the top of the chamber with a coverslip plasma-coated process for 10–20 seconds. When we put the cell into the chamber, we slid the coverslip on the top and gently introduced the swimming cell. We observed the behaviour in the condition that the chamber was completely sealed by a coverslip.

3.7 The analyses of behavioral changes in geometrical chambers

We obtained the behavioral data (center of the cell, swimming speed and cell length) according to above basically. To calculate the local staying frequency in chambers, we divided the quasi-2D physical fields by rectangular grids. Then, the probability density $p(x_i, y_j)$ in each grid was obtained from the number of observed centers of the cells in each grid. $p(x_i, y_j)$ was normalized.

Adhesive spots of the cells, duration times and the directions of anterior end adherence were manually extracted from the sequential images. Crescent areas are defined as the region within 1 mm from the tip of the crescent. And I defined analysis area of adhering cell in narrowness as inside between the rod-like structures and chambers wall. We did not count the cells staying for less than 10 s as adhesion. All statistical analyses were conducted in Python 3.7.1 using the "scipy.stat" package version 1.1.0.

3.8 Quantification of the reversal of swimming direction

I obtained a time series of swimming vectors $\boldsymbol{v}_i$ as above same manner. Then I calculated the inner product of swimming vector $\boldsymbol{v}_i$ dot $\boldsymbol{v}_{i+1}$, where i is recording frame (4 fps). The thresholds of reversal are -0.8 in corner chamber and -0.85 in star-like chamber, respectively. More than 20 times reversal in one trial is eliminated.

4 Result 1: Quantifications of behavioral changes in *S. coeruleus*

In this section, I introduce the overview of the behaviours of *S. coeruleus*. The cell changes its state accompanied by shape change. So, I explain the quantifications of behaviours and behavioural transition obtained by time series of behaviour. Then, I compared the classification of 3 types of cell states manually and statistically. Additionally, I characterized four types of behavioural transition, focusing on these shape changes. Finally, I describe the transition from the swimming state (cone shape) to the adhering state (trumpet shape) that we focus on in the thesis. These results are basically described in Echigoya et al. 2022 (Echigoya et al., 2022).

4.1 Cell behaviors in simple environment

After placing the cells in the chamber, we recorded their behavior in a quasi-2D disk chamber to quantitatively measure swimming speed and cell length over 25 minutes. The cell exhibited three shapes and behavioral transitions between these states (droplet, cone and trumpet) (Figure 4-1A), consistent with previous descriptions (Tartar, 1961). In our experiments, some cells frequently changed states (Figure 4-1B, Cell A), while others remained in a steady cone state (Figure 4-1B, Cell B). There was variation in the frequency of state changes among cells in this situation (Figure 3-3). Subsequent analyses utilized the behavioural data containing these states. We observed that cone-shaped cells accounted for 72.3% of cells, while trumpet-shaped cells accounted for 25.7%. Droplet-shaped cells were rarely observed in 2.0% (Figure 4-2, Figure 4-3). The distributions of normalized length in each state (cone = 1) are distributed to three regions (Figure 4-2). Cone-shaped cells exhibited free swimming, while droplets and trumpet-shaped cells mostly adhered or swam slowly. Then, the behavioral data are then plotted on a 2D state field in Figure 4-4A. The plot shows three main clusters corresponding to each state. The vectors in the 2D field represent the velocity of the behavioral change, allowing for quantitative evaluation of cell states and transitions (Figure 4-1A) and describing the behavioral flows between the cell states. However, transitions from droplet to trumpet and from trumpet to droplet followed the same path in opposite directions in the state field, leading to canceled and underestimated velocities regarding behavioral changes. Hierarchal clustering analysis, which connects the nearest clusters or dots repeatedly to form several clusters, was conducted on the dots in the steady cell states (Figure 4-4B). When the computational clustering divided the cell state into three, the result corresponds to the classification in manual clustering (Figure 4-4).

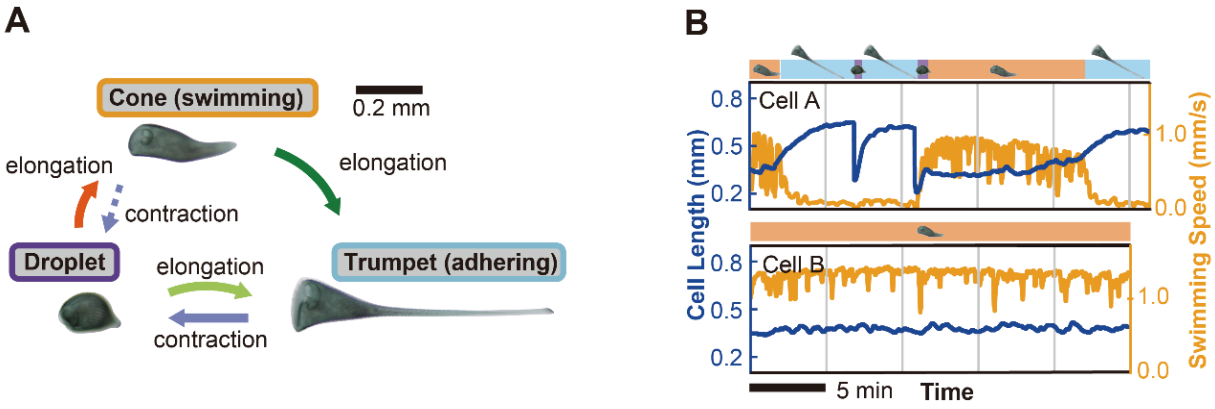

Figure 4-1 Three modes and transitions of *S. coeruleus* and the variety of behavioral modes in the quasi-2D disk chamber.

(A) Schematic images of the cell states and the transitions. (B) The time series of cell length (blue line) and swimming speed (orange line). The graph displays the typical behaviors of two cells (Cell A, B). The cell states are shown on the top of each graph.
*Created by modifying (Echigoya et al., 2022) (© 2022 Echigoya, Sato, Kishida, Nakagaki and Nishigami (Licensed under CC BY 4.0)) https://creativecommons.org/licenses/by/4.0/

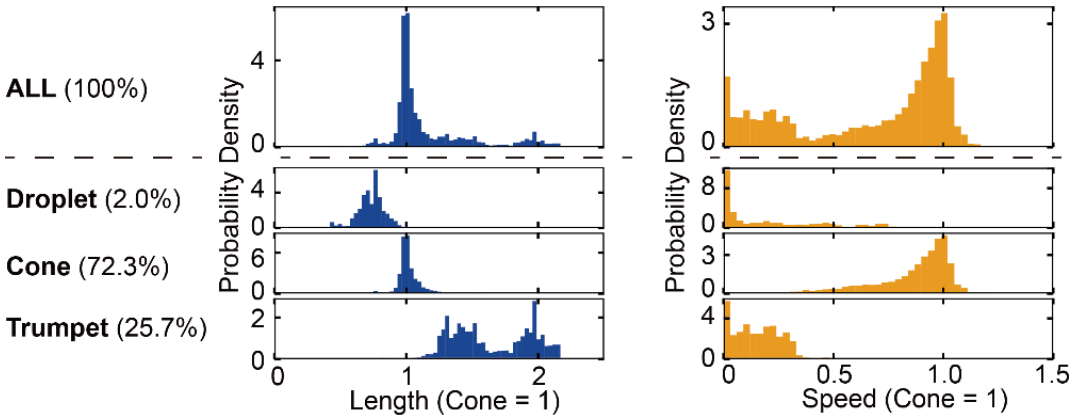

Figure 4-2 The frequency of the cell state and the distributions of the cell length and speed in each state.

The states were manually divided into droplet (2.0%), cone (72.3%), and trumpet (25.7%). The length and speed distributions were normalized using averaged values in the cone state. Droplet lengths were shorter than those in the cone state, while trumpet lengths were higher. Swimming speed was separated into the swimming state (cone) and the adhering or lower swimming state (droplet and trumpet).
*Created by modifying (Echigoya et al., 2022) (© 2022 Echigoya, Sato, Kishida, Nakagaki and Nishigami (Licensed under CC BY 4.0)) https://creativecommons.org/licenses/by/4.0/

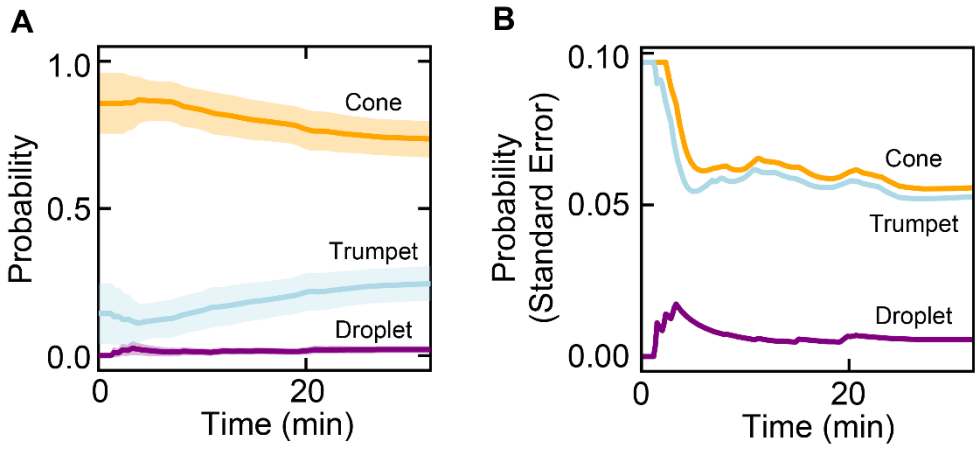

Figure 4-3 Time series of averaged probabilities and standard errors of each state from the onset of the record.

(A) Solid lines indicate the average probabilities of cell states, with transparent areas indicating standard errors for 14 cells. (B)These standard errors remain steady after 5 minutes.
*Created by modifying (Echigoya et al., 2022) (© 2022 Echigoya, Sato, Kishida, Nakagaki and Nishigami (Licensed under CC BY 4.0)) https://creativecommons.org/licenses/by/4.0/

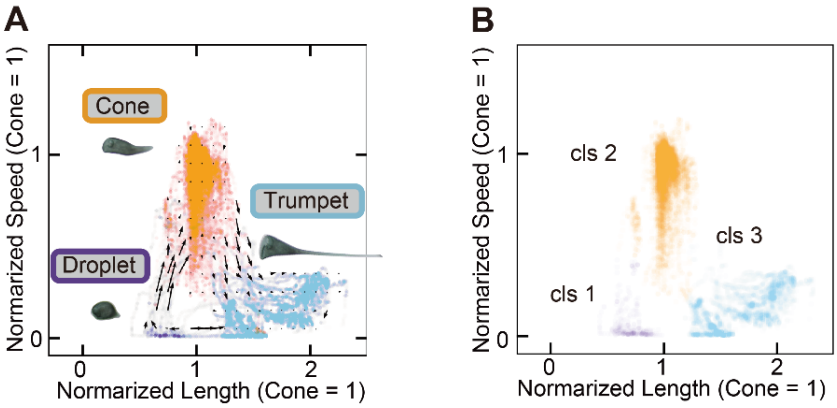

Figure 4-4 The flow of cell state transitions and the clustering of steady cell states.

(A) The transition vector of the cells is represented, with dots indicating cell states in a 2D field containing cell length and speed at different time points. The dots were manually classified into three (droplet, cone, trumpet). Hierarchical clustering of the steady cell states is also shown in (B), with dots in the 2D state field divided into three clusters, similar to manual classification.
*Created by modifying (Echigoya et al., 2022) (© 2022 Echigoya, Sato, Kishida, Nakagaki and Nishigami (Licensed under CC BY 4.0)) https://creativecommons.org/licenses/by/4.0/

4.2 Cell transition accompanied by cell deformation

To characterize the behavioral transitions accompanied by the shape deformations shown in Figure 4-1A, Figure 4-4A, we analysed the time series of the cell length and estimated the duration times of each shape deformation (Figure 4-5). The duration of each transition was estimated by

fitting an exponential function to the averaged time series of the deformation rate. Due to the rarity of the contraction process from cone to droplet (observed only three times in over 6 hours of recording), this process was excluded from the analysis. Consequently, *Stentor* exhibited a droplet shape following contraction from the trumpet shape. Then, the contracted droplet cell transitioned into cone shape and swam away (Figure 4-5A) or became trumpet shaped again (Figure 4-5C). The duration times for these transitions were 16.2 ± 0.2 s (SD, n = 13, 10 cells, Figure 4-5B) and 40.1 ± 0.51 s (SD, n = 10, eight cells, Figure 4-5D). Another elongation process from cone to trumpet is shown in Figure 4-5E, with a duration time of 107.9 ± 1.47 s (SD, n = 20, 14 cells, Figure 4-5F). In contrast, the contractile process from trumpet to droplet occurred very quickly, more than ten thousand times faster than other transitions (Figure 4-5G). In the contraction process, a two-mode exponential function (Moriyama et al., 1998) fit well [2.1 ± 0.51 ms and 15.6 ± 2.3 ms (SD, n = 8, eight cells, Figure 4-5H)] to the averaged deformation rate rather than the function with a single time scale.

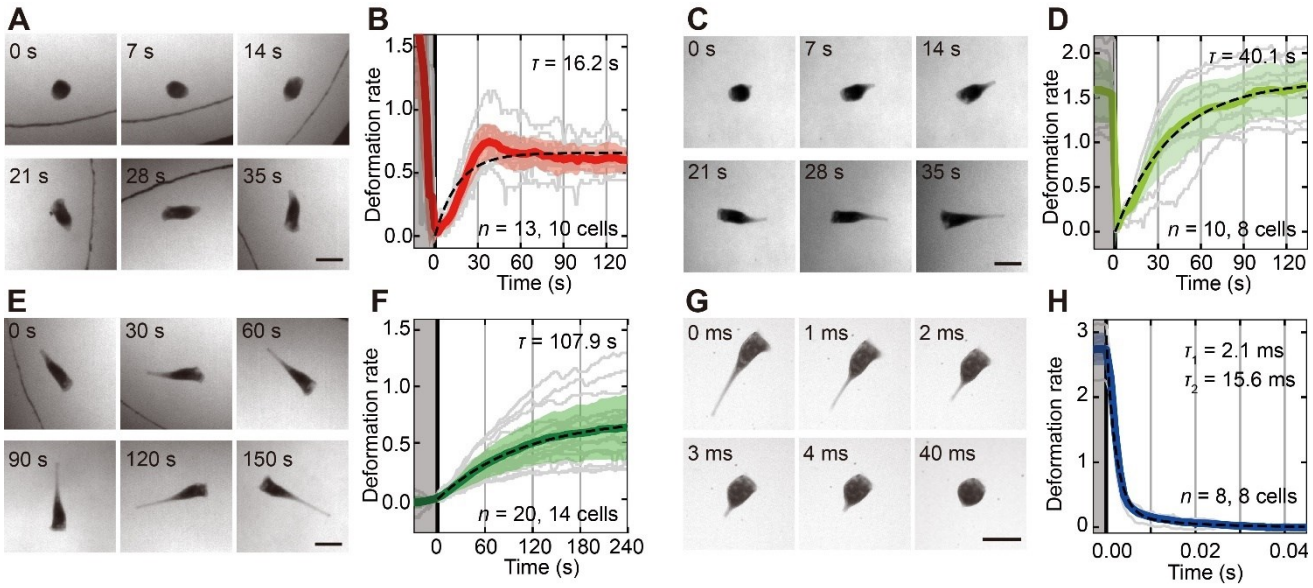

Figure 4-5 Shape transitions between cell states and the estimation of duration times for each transition.

(A,C,E,G) Sequential images of shape transitions from droplet to cone, droplet to trumpet, cone to trumpet, and trumpet to droplet are provided. (B,D,F,H) Time series of shape deformation rates and estimated duration times for each transition are also shown. Transition duration times were estimated using exponential fitting to the averaged deformation rate.

4.3 Behavioral transition from cone to trumpet

This section focuses on the transition from cone to trumpet (Figure 4-5E,F) , which is relevant to determining the adhering location. In this transition, the swimming speed decreased while its

length increased (Figure 4-6). The correlation between the length and speed of the cell showed a negative correlation, with two distinct relationships observed during the transition based on scaling methods ($s \sim l^{-6.3}$ and $s \sim l^{0.2}$, Figure 4-6B). In this process, the swimming trajectory changed from straight forward to rotating (Figure 4-7). The trajectories in the swimming and trumpet states are shown in Figure 4-8A,B. The diameter of the trajectory in the free-swimming cone state could not be measured accurately because the cone-shaped cell usually swims in a straight trajectory and there is restriction of the observation area. The diameter of the rotating trajectory of the trumpet cell (Figure 4-8B) was distributed at 1.4 ± 0.3 mm (SD, n = 133, 11 cells, Figure 4-8C). Furthermore, the parameters of the beating forms of the membranellar band differed between the cone state and trumpet state (Figure 4-9).

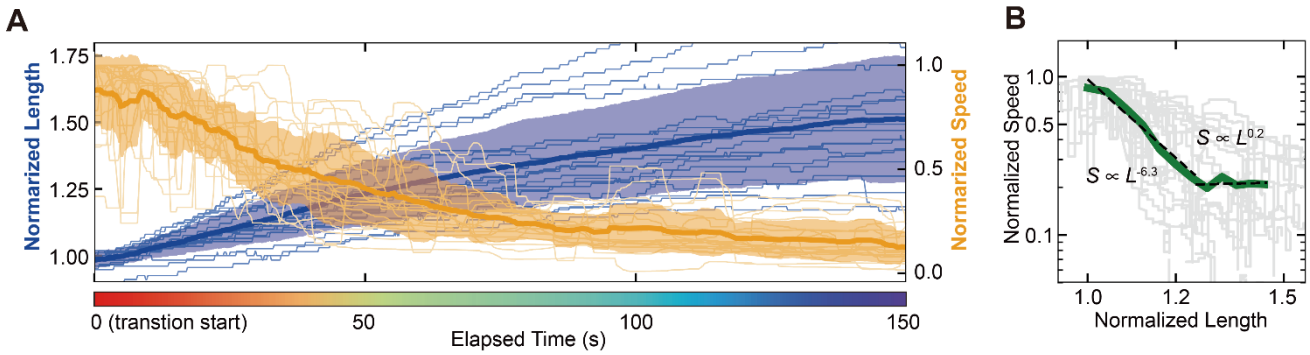

Figure 4-6 behavioral transition from swimming (cone-shaped) to adhering (trumpet-shaped).

(A) Time series of the cell length (blue line) and swimming speed (orange line) during this transition, with solid bold lines representing averaged data and solid thin lines representing individual data. Transparent regions indicate standard deviations. These values are normalized by setting Cone = 1, revealing a negative correlation between cell length and swimming speed. (B) The correlation between cell length and speed is further detailed. The green solid line represents the average speed, while gray lines depict individual transition data. The averaged data are fitted by power laws, showing characteristic factors of −6.3 in the range of 1–1.25 (normalized length) and 0.2 in the range of 1.25–1.45 (normalized length).

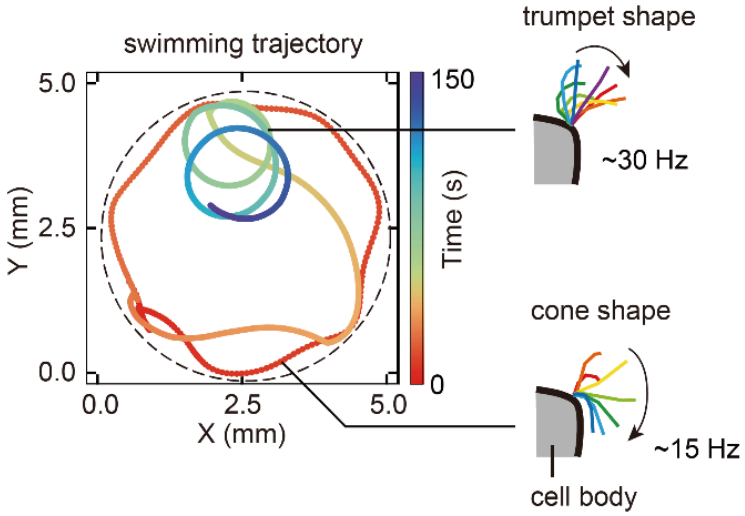

Figure 4-7 The trajectory of a cell and beating forms in the behavioral transition from swimming to adhering.

As the cell elongates, the cell becomes locally rotating. The color represents elapsed time from the beginning of the transition. The dashed line represents the wall of the chamber. In behavioural changes, beating characters occur between each state.
*Created by modifying (Echigoya et al., 2022) (© 2022 Echigoya, Sato, Kishida, Nakagaki and Nishigami (Licensed under CC BY 4.0)) https://creativecommons.org/licenses/by/4.0/

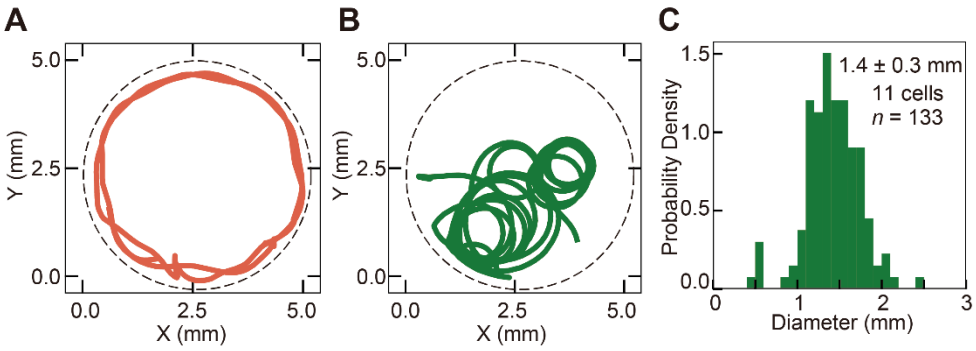

Figure 4-8 The comparison of trajectories between cone state and trumpet state.

(A,B) The comparison between the swimming trajectories at swimming steady state and steady rotating state. The distribution of the swimming pass diameter in the steady rotating state is shown in (C), with a diameter of 1.4 ± 0.3 mm (SD, n = 133, 11 cells).
*Created by modifying (Echigoya et al., 2022) (© 2022 Echigoya, Sato, Kishida, Nakagaki and Nishigami (Licensed under CC BY 4.0)) https://creativecommons.org/licenses/by/4.0/

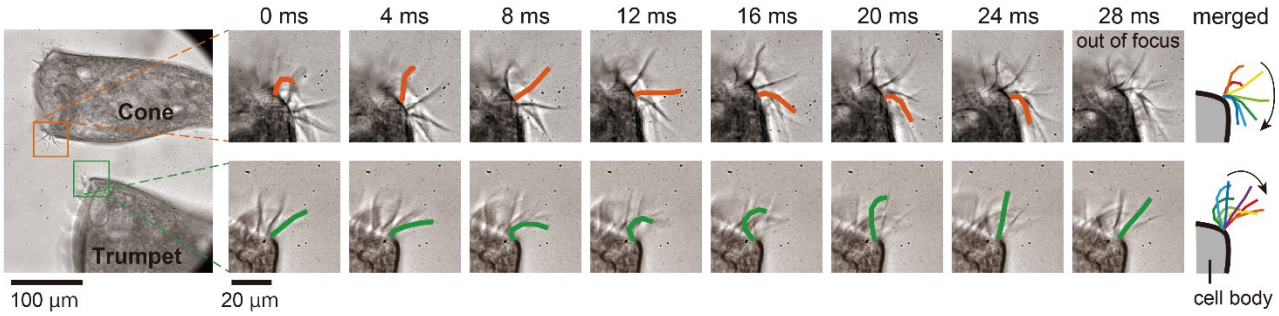

Figure 4-9 The difference in the beating forms of the ciliary band (membranellar band) in *S. coeruleus* in cone and trumpet states.

Cells collected from the Shiribetsu River were cultured and observed after washing with fresh modified Peters' solution. The beating forms were observed using an inverted microscope and recorded at 2,000 fps. Beating frequencies were approximately 15 Hz in the cone state and 30 Hz in the trumpet state, with angles of approximately 130 degrees in the cone state and 70 degrees in the trumpet state. These differences may contribute to the switching motility from a straightforward swimming trajectory to a rotating one.
*Created by modifying (Echigoya et al., 2022) (© 2022 Echigoya, Sato, Kishida, Nakagaki and Nishigami (Licensed under CC BY 4.0)) https://creativecommons.org/licenses/by/4.0/

5 Result 2: Adhering behavior influenced by geometrical cues

I describe the transition of the cell in the previous section. Then, when do the transitions occur? In this section, I explain the behavioural transition influenced by an obstacle in the chamber. After that, the trumpet-shaped cell attaches to narrow areas formed by an obstacle and chamber wall, and then the cell feeds bacteria or small ciliate, causing feeding flow (These results are basically described in Echigoya et al. 2022 (Echigoya et al., 2022)). Next, we examine the selection of anchoring locations depending on surrounding geometrical parameters. I made several observation chambers consisting of several narrow areas and showed where the cell adheres. Lastly, we explain the analysis of behaviours focusing on the motility constraint by surrounding geometry related to behavioural transitions.

5.1 Behavioral change influenced by extracellular structures

In nature, *Stentor* elongates and adheres to more favorable locations for better living conditions, acquiring information about the external environment in the process. To determine where they tend to adhere, we focused on the geometry in the outer swimming environment and observed their behaviors in the quasi-2D gel chambers designed to promote cell adhesion with/without the structure (Figure 5-1A).

The presence of structures in the chamber influenced the frequency of cell states. In the chamber without the structure (control), the cell mainly took the cone state in 74.1%, while the trumpet and droplet states were observed for 22.4% and 3.5%, respectively (Figure 5-1B). However, in chambers with structures, cells dominantly took on a trumpet shape (72.4%) or a droplet shape (10.7%), with cone-shaped cells accounting for only 16.9% (Figure 5-1B). In chambers with structures, trumpet- and droplet-shaped cells tended to adhere, and swimming cells often collided with the structures, leading to a distribution of lower swimming speeds (Figure 5-2A,C). The average frequencies in each state had significant differences in Welch's *t*-test ($p = 0.0026$ in droplet, $p = 6.3 \times 10^{-7}$ in cone, $p = 2.0 \times 10^{-6}$ in trumpet, Figure 5-1C), indicating that the geometry of the external environment influenced the modulation of their states.

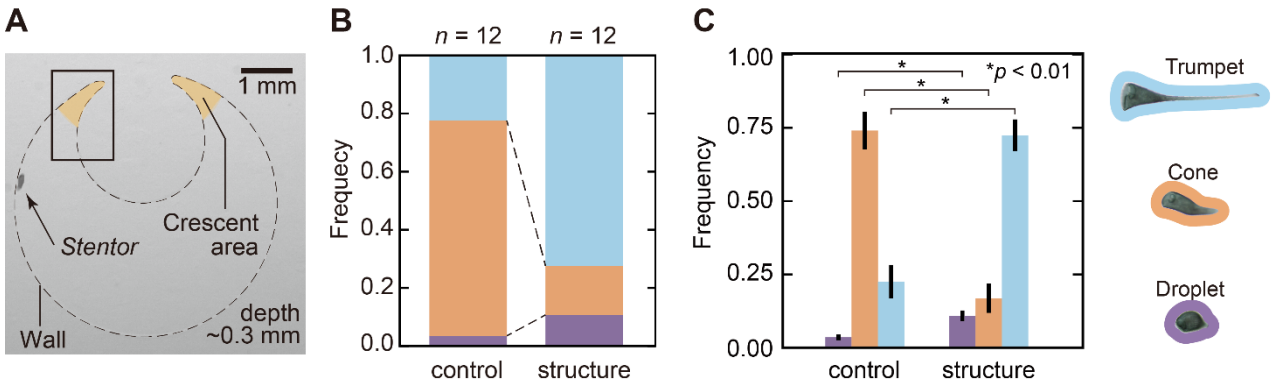

Figure 5-1 The influence of the structure on cell states.

(A) The geometry of the gel chamber containing the structure, with dashed lines representing the chamber walls and orange regions indicating crescent areas. (B) In the control chamber without the structure, the cell mainly takes the cone state (74.1%), with trumpet (22.4%) and droplet (3.5%) states also present. In contrast, the chamber with the structure sees the cell predominantly in a trumpet shape (72.4%) and a droplet shape (10.7%), with cone-shaped cells observed in only 16.9% of cases. (C) The difference in state probabilities between the simple and structured chambers with significant differences indicated by Welch's t-test, ($p = 0.0026$ in droplet; $p = 6.3 \times 10^{-7}$ in cone; $p = 2.0 \times 10^{-6}$ in trumpet). The bars represent standard errors (12 cells).

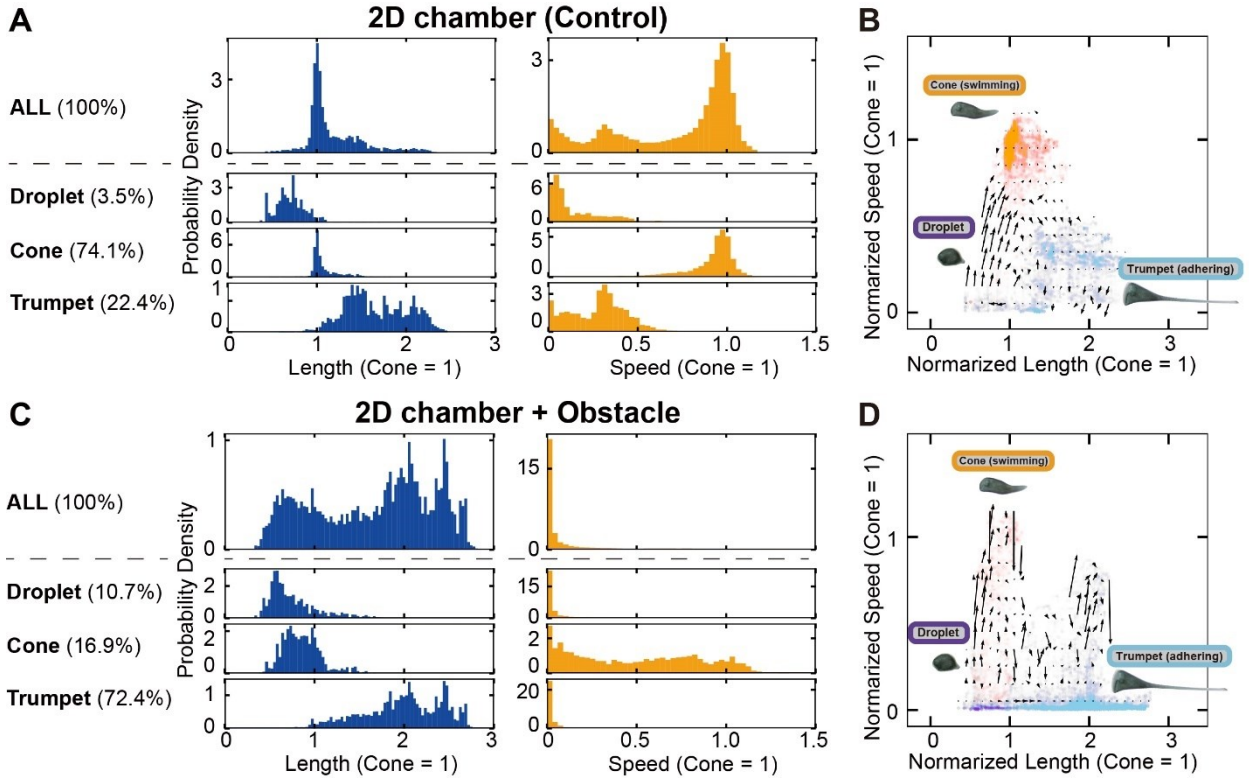

Figure 5-2 The frequencies of cell states and transition vectors in the quasi-2D gel chamber with and without a structure.

(A) The frequency of cell states and distributions of cell length and speed are shown for each state, derived from observations of 12 cells over approximately 40 minutes. Manual classification by Tartar's descriptive classification shows 3.5% droplets, 74.1% cones, and 22.4% trumpets without a structure. (B, D) Transition vectors of the cell in the 2D 'physical' state field with dots manually classified into droplet (purple), cone (orange), and trumpet (light blue) states. These values are normalized by setting cone = 1. In (C), the frequency measured by observation time of each cell state and the distributions of cell length and speed in each state are shown for observations with a structure, indicating 10.7% droplets, 16.9% cones, and 72.4% trumpets.

5.2 Anchoring behavior at narrow regions effected by a geometrical cue

The 2D color maps in Figure 5-3A,B represent the averaged probability densities of the cell's position in each chamber. In the quasi-2D chamber without a structure, the probability density was uniformly distributed along the wall (Figure 5-3A). Conversely, the cell frequently stayed between the wall and the structure, referred to as crescent areas (in the orange area in Figure 5-1A) (Figure 5-3B). The presence frequencies in swimming state were 614.9 ± 136.6 s/mm^2 (SE, n = 12, 12 cells) in crescent areas and 43.4 ± 11.1 s/mm^2 (SE, n = 12, 12 cells) in other regions. Welch's t-test

indicated a significant difference between them (p = 0.0015, Figure 5-3C), suggesting an increased presence in the crescent areas.

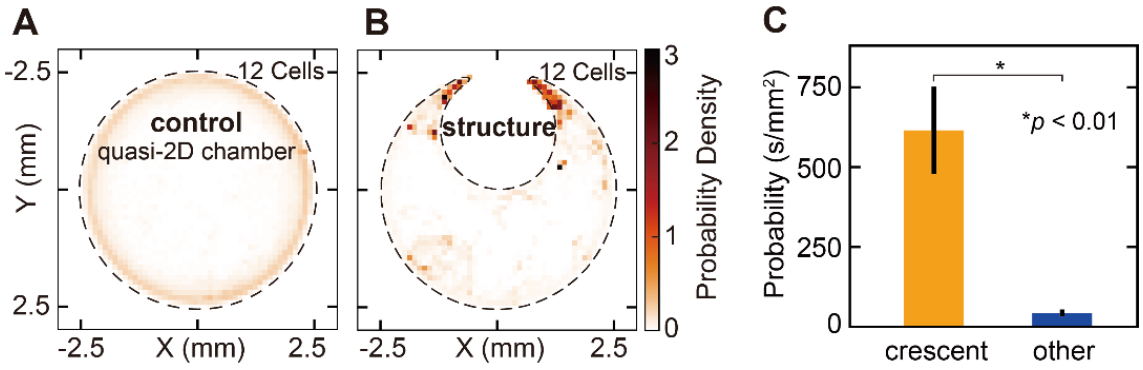

Figure 5-3 The comparison of swimming *Stentor* influenced by a structure in the chamber.

(A,B) The 2D maps of probability density in each chamber. (C) The comparison of presence probability within the crescent areas and other regions. The presence probabilities, excluding adhering, are 614.9 ± 136.6 s/mm^2 (SE, n = 12, 12 cells) in crescent areas and 43.4 ± 11.1 s/mm^2 (SE, n = 12, 12 cells) in other regions. The difference is statistically significant in Welch's *t*-test. Black bars are standard errors.

Our experiment indicates that cells tend to stay in and adhere to the crescent areas. Figure 5-4A shows the positions and duration times of adhesion in 12 cells. All 12 cells adhered to the substrate in chamber with the structure. Although two cells did not adhere to the crescent areas, the remaining 10 cells exhibited switching behavior from swimming to adhesion (from cone to trumpet) in the crescent areas. In these 10 cells, 9 cells maintained their feeding (trumpet state) with the oral structure directed opposite to the dead end (Figure 5-4B, Figure 5-5C). While the adhering frequency in crescent areas (28.0 events/mm^2) was higher compared to other regions (0.9 events/mm^2), the difference between adhering times per cell prior to the detachment (603.0 ± 209.2 s (SE, n = 18, 10 cells) in crescent areas and 411.2 ± 187.1 s (SE, n = 13, seven cells) in other regions) were not significant in Welch's *t*-test (p = 0.50; Figure 5-4C).

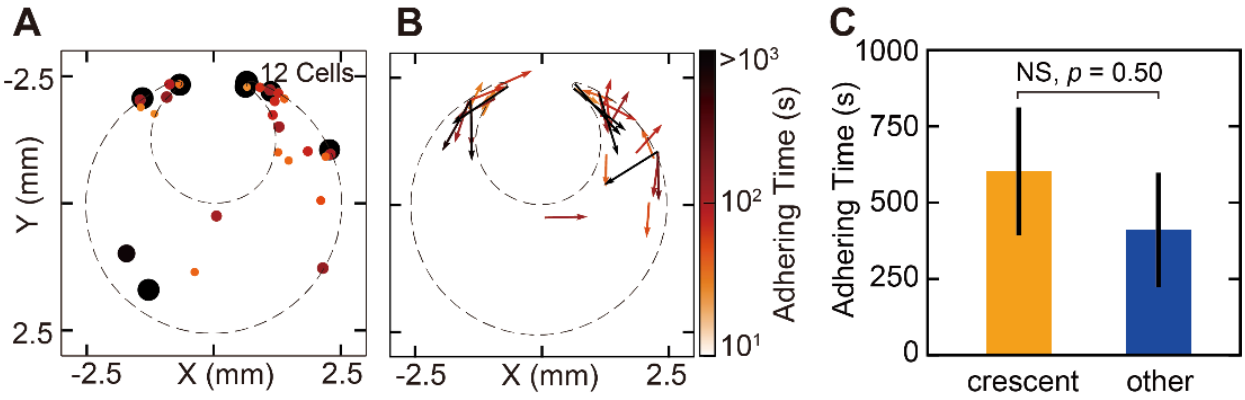

Figure 5-4 Adhering behavior in the chamber with an obstacle.

(A) The locations and duration times of adhesion in the cell. The color and size of the dots represent the duration of adhesion. The color bar represents the logarithmic adherence time scale. (B) The directions of the cell in the adhesive state. The color and length of the vectors represent the adhering time in one direction. (C) The comparison of adhering time prior to the detachment within the crescent areas and other regions. Ten cells adhered in crescent areas (18 events) and 7 cells adhered in other regions (13 events) in observed 12 cells (31 events). The averaged adhering times prior to detachment are 603.0 ± 209.2 s (SE, n = 18, 10 cells) in the crescent areas and 411.2 ± 187.1 s (SE, n = 13, seven cells) in other regions. Welch's t-test revealed that they did not have a significant difference (p = 0.50). Black bars are standard errors.

Figure 5-5A–C shows typical sequential images of the adhesion processes in the crescent area. Initially, the cell encountered the crescent area and moved back and forth (Figure 5-5A). Then, the posterior region briefly elongated and contacted the wall, sometimes swam backward. Eventually, the posterior region adhered to the substrate and elongated over 1–2 minutes (Figure 5-5B). Occasionally, bending behavior could be observed (sequential images from 96 to 120 s in Figure 5-5B). Although contraction and elongation between the trumpet and droplet state occured, the cell typically remained adherent at the same location for more than 35 min (Figure 5-5D, Figure 5-6).

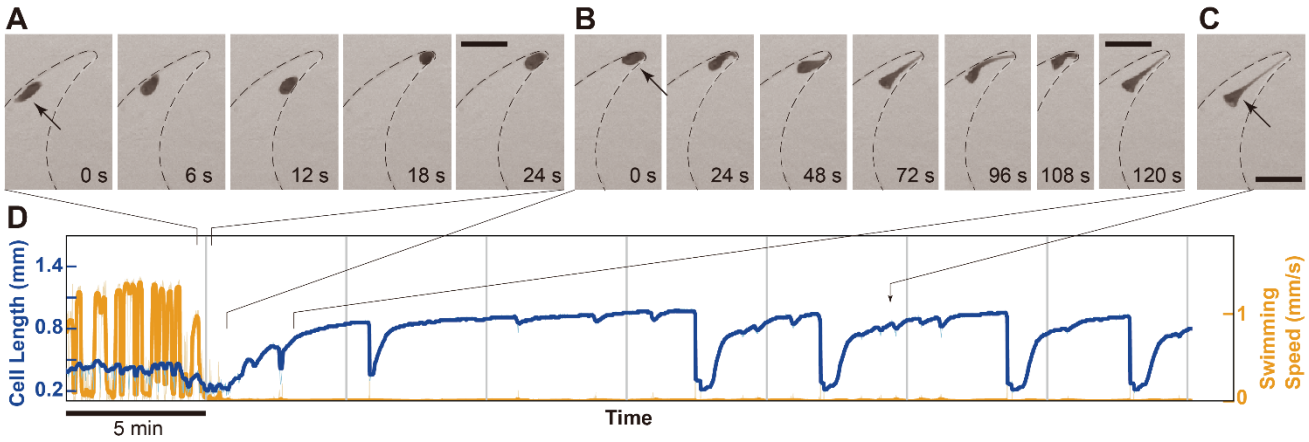

Figure 5-5 Typical sequential images of the process from swimming to adhesion in the crescent area.

(A) The cell entering the crescent area before adhering. (B) The transition of adhesive cells from cone-shaped to trumpet-shaped. (C) The cell adhering and feeding in the crescent area. The direction of the anterior end directs toward the opposite side of the dead end. All bars are 0.5 mm. (D) The time series of the cell length and swimming speed in the process from swimming to adhesion in the crescent area. Images in (A)–(D) represent the sections in the graph.

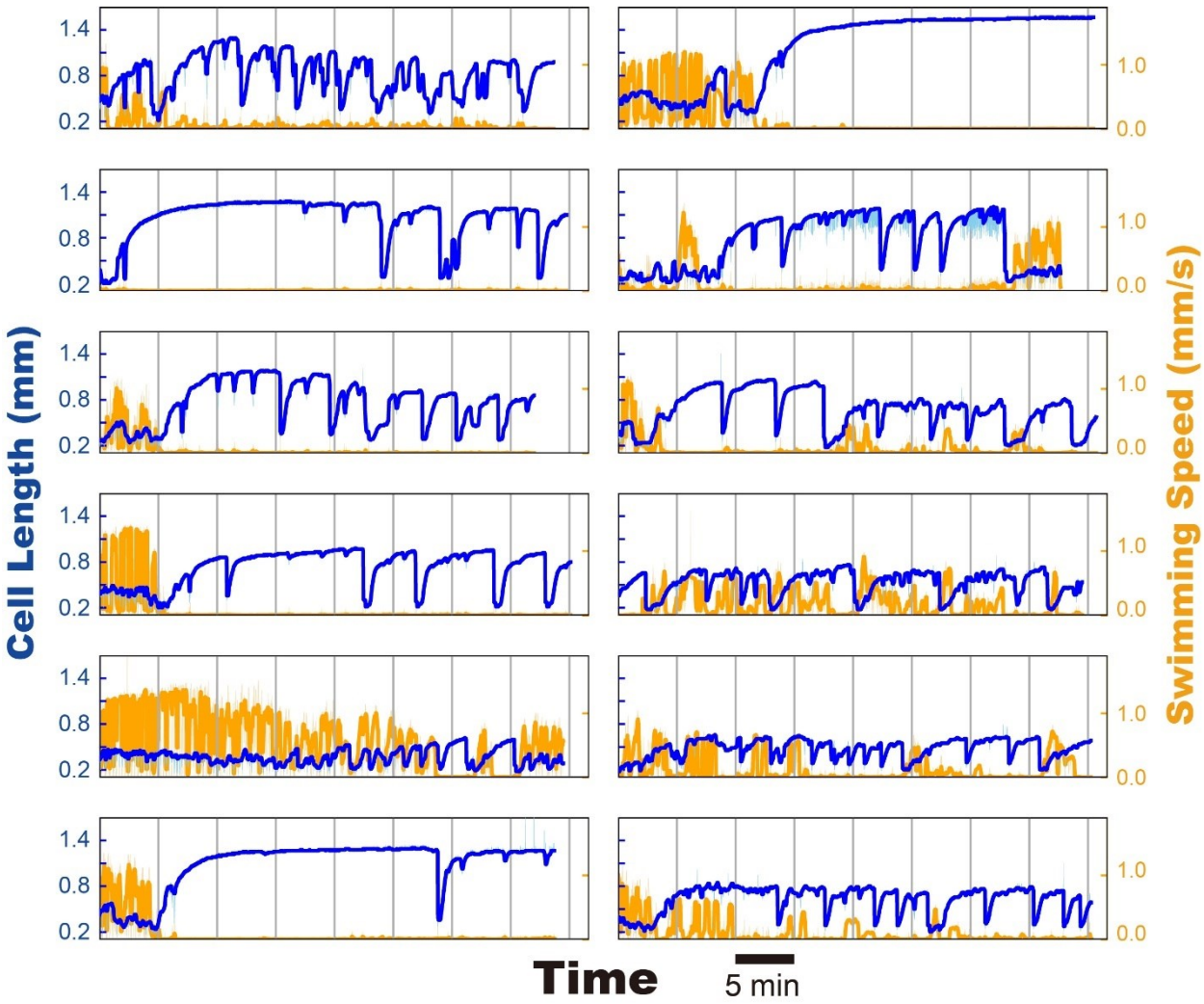

Figure 5-6 The time series of the cell length (blue) and swimming speed (orange) in the chamber with the structure.

The modulation of cell states is influenced by the structure in the arena. In the crescent areas, the cell not only stays frequently but also switches its behavior and adheres for extended periods with its oral structure directed opposite to the dead end.

5.3 Selection of anchoring locations effected by geometrical parameters

Anchoring locations in *S. coeruleus* are affected by geometrical parameters forming narrow regions. The cell swam around the chamber containing four specific regions formed at different angles (30, 45, 60 and 90 degrees, named "angle chamber", Figure 5-7A). Figure 5-7B shows the frequency distribution of the position in 12 swimming cells. *S. coeruleus* tended to swim along the wall and was found in the corners formed by wall and rod-like structures. Presence rates in 4 narrow areas are shown in Figure 5-7C. The rate in a 90-degree location was highest, and the rate in a 60-

degree area was lowest. We consider that both sides in 90-degree rods make the bias. We also consider that the rod's order affected the bias because each rod-like structure guides the direction of the swimming cell (Figure 5-7B). Then, the cell adheres to some location.

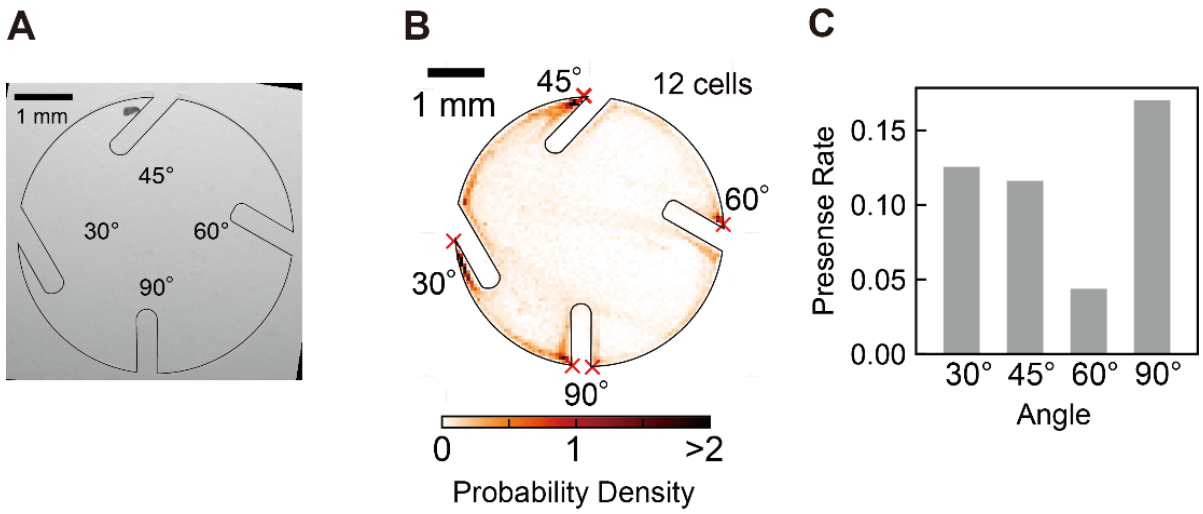

Figure 5-7 Swimming behaviour of *Stentor* in a geometrical chamber about angle.

(A) The geometry of observation chamber in top view. There are 4 types of corners formed by the chamber's wall and rod-like structure. (B) two dimensional distibution about the locations of the 12 swimming cells. The dense color in narrowness and along the wall represents a high frequency of the presense. (C) Quantifications of presense rate at each angle. Presense rate means the ratio of time in the presense at each corner divided by all observation time.

Dots in Figure 5-8A represent the adhering positions, and the dots' size (and colour) means duration time (12 cells, 22 adhering events). *Stentor* tended to anchor to narrow areas at 30 and 45 degrees. By quantifying adhering duration time in each narrow area (Figure 5-8B), total adhering time in 30 and 45-degree areas was higher than others. These results in Figure 5-8B show some bias about presence rates and area in each region. In order to eliminate the biases, we obtained the ratio of total adhering time to total presence time in each narrow area (Figure 5-9A) and total adhering time per area (Figure 5-9B). Even though we standardized total adhering time by presence time and area, the cell tended to adhere to the region formed by a smaller angle.

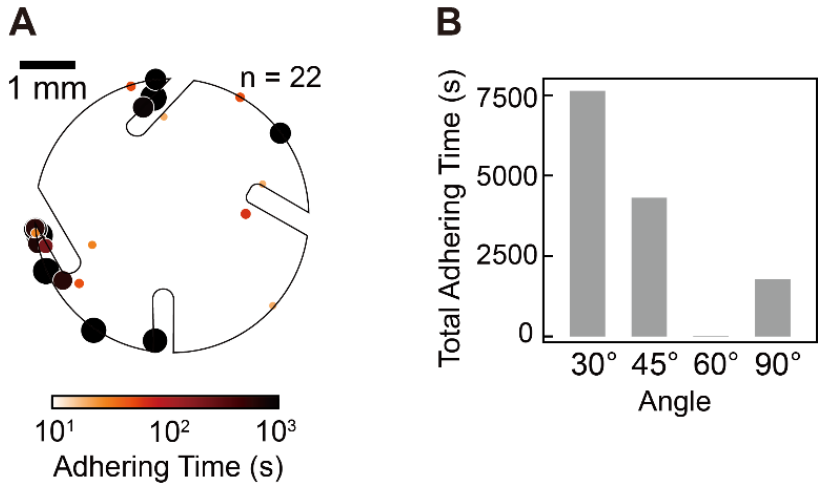

Figure 5-8 Selecting of anchoring locations in the angle chamber.

(A)Anchoring locations in 12 cells. Dots and color (area) in each dot represent the position of anchoring event and duration time, respectively. (B) Quantification of total adhering time in each corner. The cell tends to adhere to narrower region such as 30 and 45 degrees.

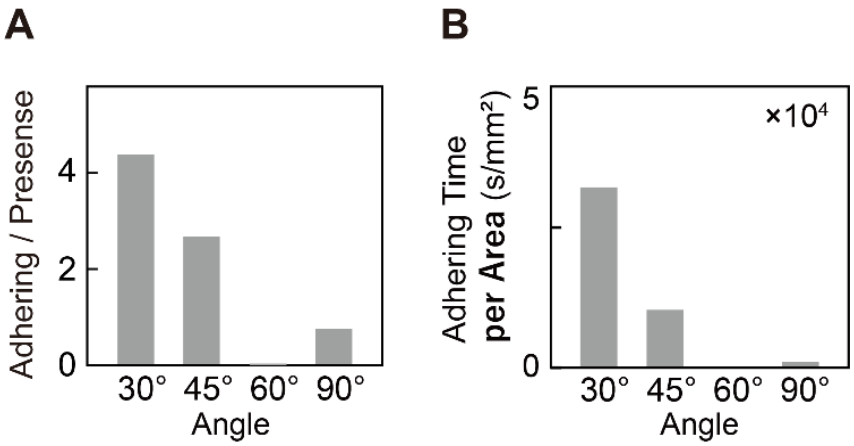

Figure 5-9 Normarization of the selecting behaviours.

Toral adhering times are normarilized by total presence times at each corner (A) and areas of corners in (B).

We observed the behaviour of one cell in the chamber containing three types of corners, in which curvature radius r (mm^{-1}) of the tip differ (named "star chamber", Figure 5-10A). In the same manner, we obtained the 2D map of presence distribution in the chamber (Figure 5-10B, 15 cells). From these results, presence rates in each corner were almost the same (Figure 5-10C). On the other hand, the cell tended to anchor to the region containing a sharper tip (Figure 5-11A, 10 cells, 19 adhering events). In this experiment, 5 cells remained swimming in our observations. Quantification of total adhering time in each corner also showed that *S. coeruleus* tends to anchor longer in areas containing sharper corners (Figure 5-11B). Figure 5-12 shows the standardization of adhering time

by presence time in each corner. The ratio of total adhering time to total presence time in corners showed that a small curvature radius affected the anchoring behaviours of *S. coeruleus*. In these results, geometrical parameters, angle, and curvature of the corner's tip forming narrow areas affect the selection of anchoring locations in the cell.

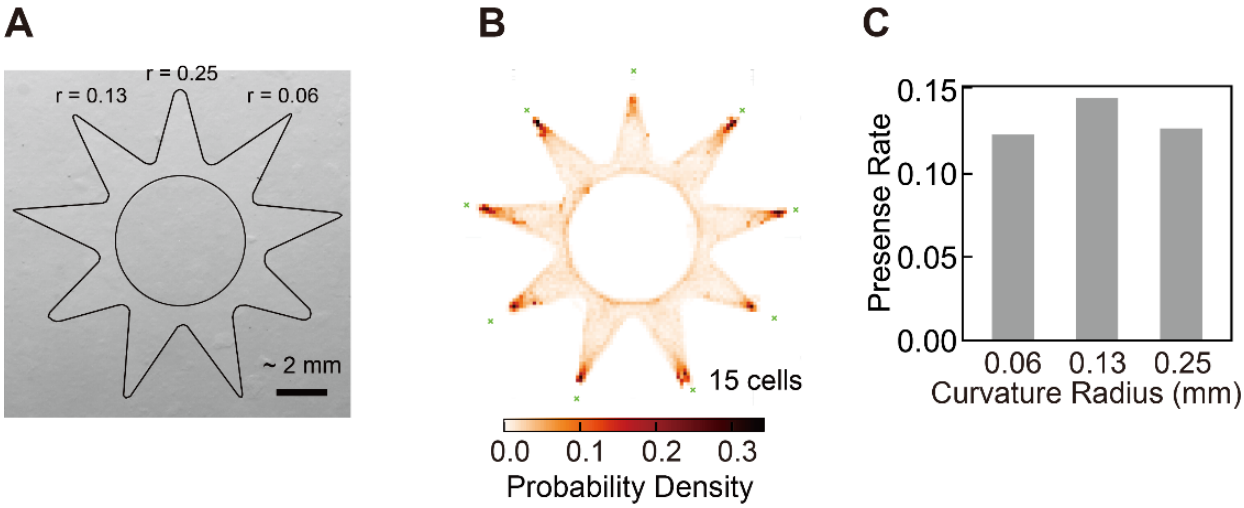

Figure 5-10 Swimming behaviour of *Stentor* in a star-like chamber.

(A) The geometry of the observation chamber in the top view. There are 9 corners containing three types of corners. Each corner tip has different curvatures. These curvature radius (mm) are 0.06, 0.13 and 0.25. (B) two-dimensional distribution about the locations of the 15 swimming cells. The dense colour in the tip of the corners represents a high frequency of the presence. (C) Quantifications of presence rate at each curvature. Presence rate means the ratio of time in the presence at each corner divided by all observation time.

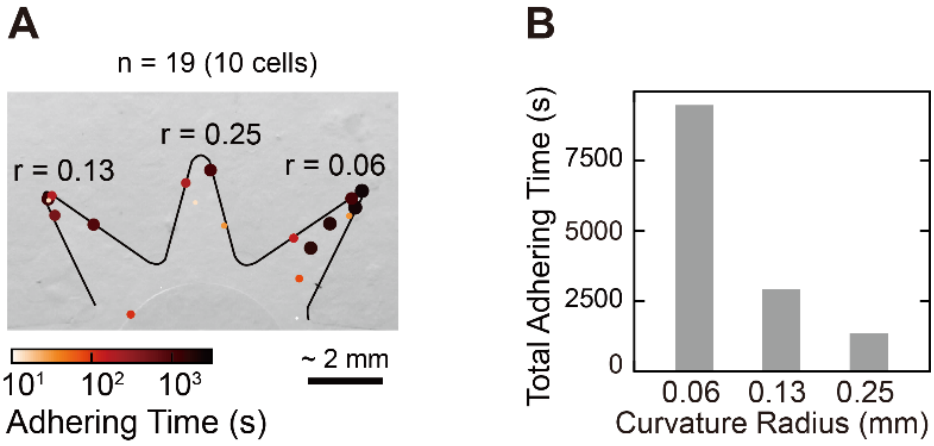

Figure 5-11 Selecting of anchoring locations in the star-like chamber.

(A)Anchoring locations in 10 cells. Dots and colour (area) in each dot represent the position of the anchoring event and duration time, respectively. (B) Quantification of total adhering time in each corner. The cell tends to adhere to a sharper region.

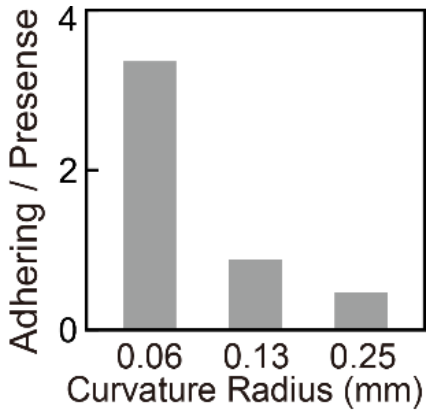

Figure 5-12 Normalization of the selecting behaviours.

Toral adhering times are normalized by total presence times at each corner.

Regarding the influence of selecting anchoring locations by the depth of narrowness, we examined using two types of chambers, and then the tendency depended on the method of quantifications. Firstly, we observed the behaviour of one cell in the chamber containing four types of narrow areas between the outer wall and different length rod-like structures (0.4, 0.8, 1.2 and 1.6 mm, named "length chamber", Figure 5-13A). Like the two types of chamber mentioned above (Figure 5-7B, Figure 5-10B), swimming cells were often observed along the chamber wall and between the wall and the structures (Figure 5-13B, 20 cells). We analysed the total presence time in each of the four areas from the cell's position and found that the cell accumulated in deeper areas (Figure 5-13C). Moreover, the cell frequently swam along specific trajectories, which we could see in the sharrow lines connecting each structure in Figure 5-13B. The order of different types of rod structures influenced the swimming trajectory and distribution of the cell position in the chamber. Figure 5-14A shows the 40 anchoring positions in 15 cells. The other 5 cells remained swimming during the observation time. The distribution of the total anchoring time (Figure 5-14B) had the same tendency as the distribution of the total presence time in each area (Figure 5-13C). The cell tended to adhere to deeper regions. Although the length of the swimming cell is about 0.4 mm, we can find the anchoring events between the wall and the shortest rod (0.4 mm), which is the same length. The narrow areas constructed with longer rod-like structures had more expansive adhering areas. To eliminate this bias, we calculated the total adhering time per adhering area (Figure 5-15B). This standardisation means that the frequency of adhering in sharrow locations is high. If the cell randomly switched from swimming to adhering, the areas where we frequently observed the swimming cell were selected as anchoring locations. To eliminate this bias, we calculated the ratio of total adhering time to total presence time in each area (Figure 5-15A). We can see the same manner as Figure 5-15B. These standardisations indicate that the wideness of anchoring areas caused the bias in selecting anchoring locations of *S. coeruleus*.

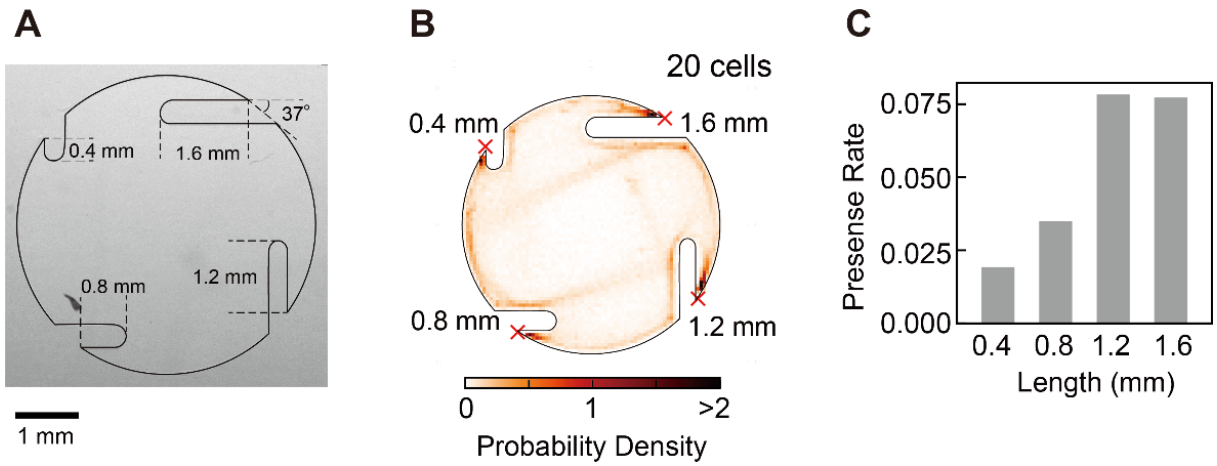

Figure 5-13 Swimming behaviour of *Stentor* in a geometrical chamber about length.

(A) The geometry of the observation chamber in the top view. Four types of corners are formed by the chamber's wall and rod-like structure. (B) Two-dimensional distribution about the locations of the 20 swimming cells. The dense colour in narrowness and along the wall represents a high frequency of the presence. (C) Quantifications of presence rate at each angle. Presence rate means the ratio of time in the presence at each corner divided by all observation time.

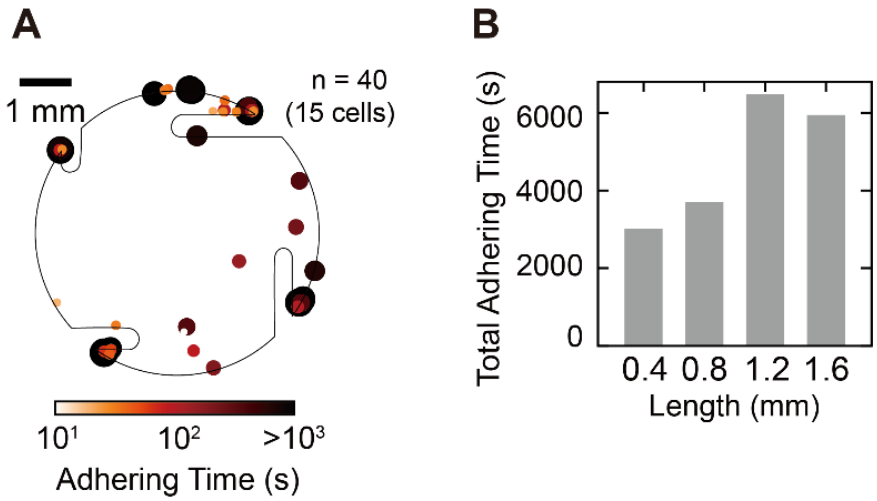

Figure 5-14 Selecting of anchoring locations in the length chamber.

(A)Anchoring locations in 15 cells. Dots and colour (area) in each dot represent the position of the anchoring event and duration time, respectively. (B) Quantification of total adhering time in each corner. The cell tends to adhere to deeper regions such as 1.2 mm and 1.6 mm.

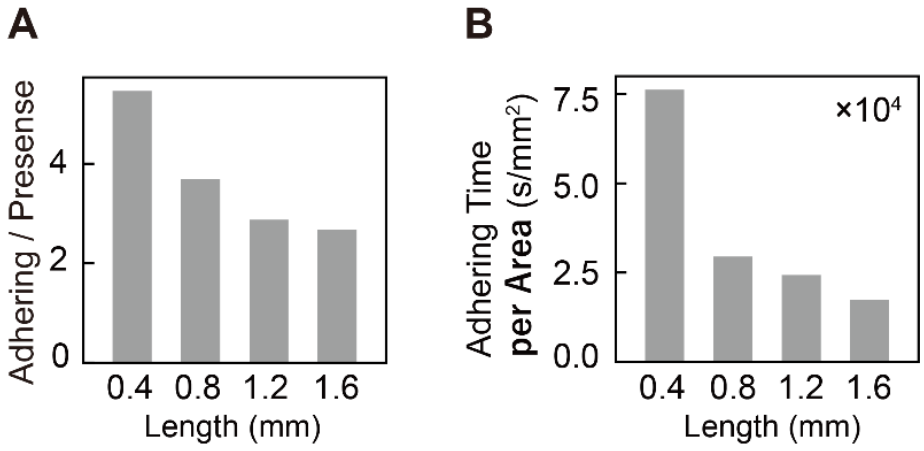

Figure 5-15 Normalisation of the selecting behaviours.

Toral adhering times are normalised by total presence times at each corner (A) and areas of corners in (B).

Secondly, we observed the behaviour in the chamber containing narrow rectangular areas, whose widths are the same (0.2 mm), and the depths are different (0.2, 0.5, 1.2 and 3.0 mm, named "sun chamber", Figure 5-16A). We can see the same tendency in the distribution of total adhering time per area in the chamber compared with the length chamber. However, we can see different tendencies of total anchoring time per total presence time. The high presence rate of swimming cells was around the outer tolas area. The cell did not come to rectangular areas. However, adhering points assembled in these rectangle areas, particularly in deeper regions (Figure 5-16B). There were 39 adhering events in 11 out of 18 cells (7 cells remained swimming). There were four types of rectangular areas, and the number of same-depth regions was four (a total of 16 rectangular areas). Figure 5-17A shows the adhering points overlapped in the same length areas. I calculated the total adhering time in each rectangular area from these data. The total adhering time in deeper regions tended to be larger (Figure 5-17B, Figure 5-18A), and the cell did not anchor to a 0.2 mm region, which was smaller than the swimming cell length. Then, we normalized the total adhering time by each rectangular area (Figure 5-18B). This result showed the depth threshold between 0.2 mm and 0.5 mm and the negative correlation between depth and adhering time per area. So, the bias of total adhering time was caused by the wideness of adhering areas. From these experiments (Figure 5-15, Figure 5-18), the depth forming narrow areas had little influence on selecting anchoring locations.

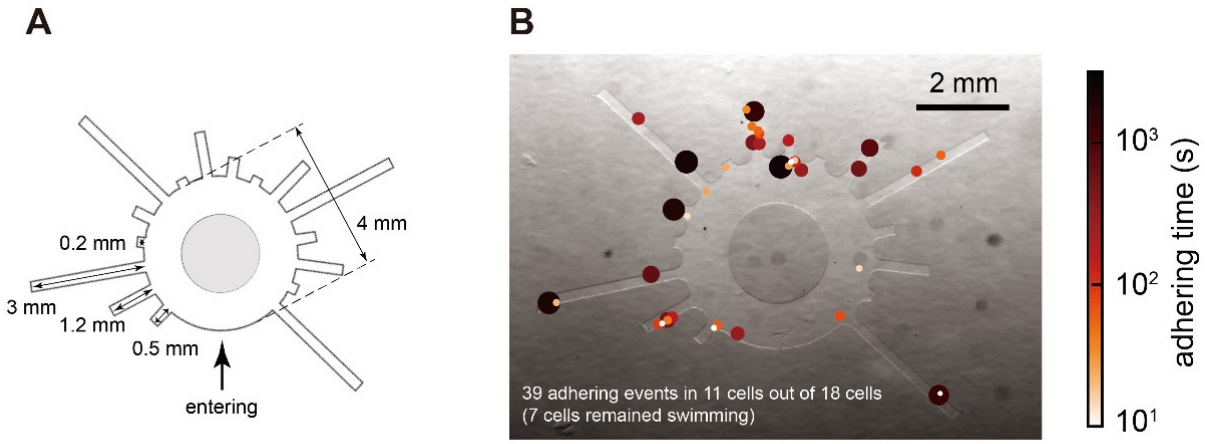

Figure 5-16 Influence of depth of narrowness to adhering behaviours.

(A) The geometry of the observation chamber in the top view. There are 16 rectangular areas containing 4 types regarding the depth. The depths of each rectangular area are 0.2 mm, 0.5 mm, 1.2 mm and 3.0 mm. (B) Anchoring locations in 11 cells. Dots and colour (area) in each dot represent the position of the anchoring event and duration time, respectively. The cell tends to adhere to rectangular areas, not broad ring areas.

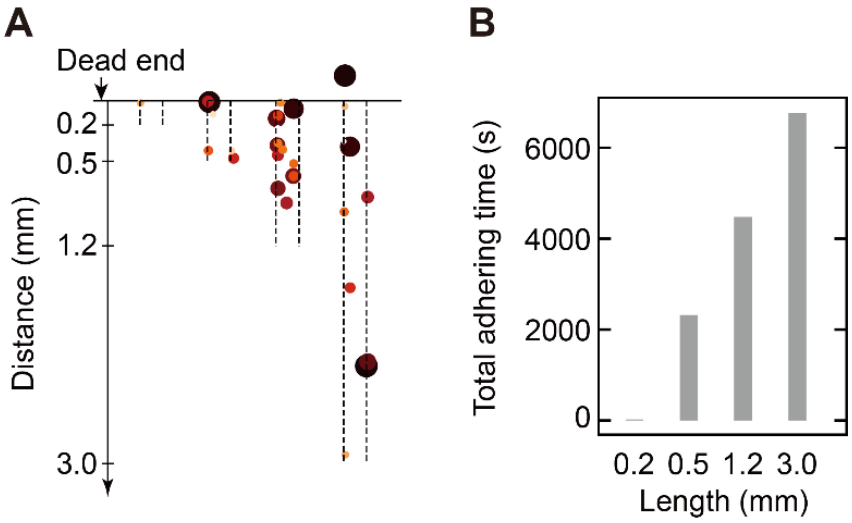

Figure 5-17 Adhering of the cell in sun-like chamber.

(A) The positions of adhering cells in each rectangular area merged 4 same rectangular areas. (B) Quantification of total adhering time in each area. There are positive correlation between depth and total adhering time.

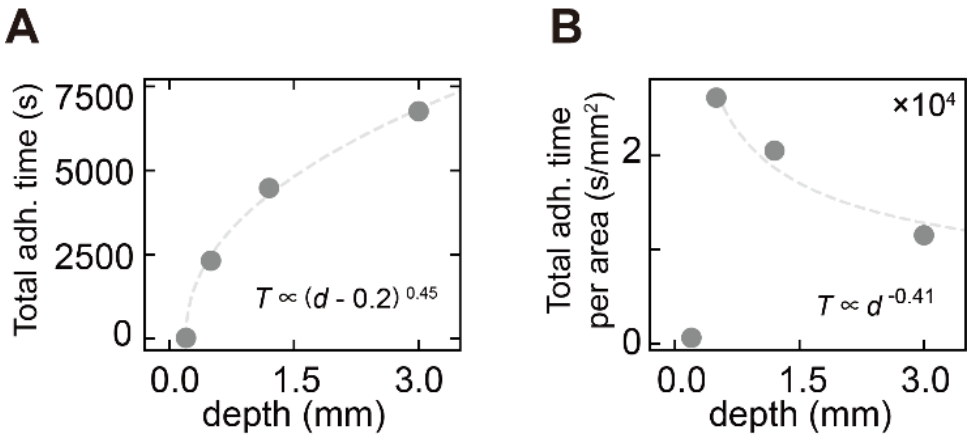

Figure 5-18 The characterization of adhering behaviour in the sun-like chamber.

The curve fitting on the total adhering time is in A, and the normalized total adhering time by area of each rectangular area is in B.

6 Result 3: Mechanisms and advantages of adhering to narrow areas.

I approach the mechanism and advantages of adhering to narrow areas in this part. I examine it from physical and intracellularly approaches.

6.1 Feeding flow at narrow regions

The flow field caused by *Stentor* was obtained by adding tracer particles to the medium. *Stentor* caused flow around the cell using cilia covering the whole cell surface for swimming and feeding. In a quasi-2D chamber, when the cell adhered to the substrate far from the wall of the chamber, symmetrical vortex flows appeared around the cell (Figure 6-1). The cells sometimes form a colony, and the colony cooperatively causes flow. The flow structure was complex, as shown in Figure 6-2. The flow interacted with the flow caused by next to the cell. The flow field shown in Figure 6-2B was obtained from the vector field in Figure 6-2A.

Next, I measured the flow field of the adhering cell at several types of corners. These corner angles are 18, 30 and 45 degrees. The attaching cell at the corner tip formed flow structures, and I recorded the motion of tracer particles at four focal planes and obtained flow fields from these records (Figure 6-3). In wide corners (30 and 45 degrees), we can see the vortex flow next to the anterior of the cell at each focal plane. On the other hand, directional flows were caused at each focal plane in the narrow corner (18 degrees). The continuum equation constrains the fluid motion. When the flow from anterior to posterior causes, reversal flow from posterior to anterior must be created hydrodynamically. In the narrow corner at 18 degrees, the flow came into the corner at the bottom, and the flow came out at the top. In wide corners, vortex flow was consistent with the constraint.

The corner angle affected the flow field caused by the cell that attached near the wall. However, when the angle of the corner changes, the aspect ratio also changes (depth and distance between the anterior and wall). In addition, the position of the cell "mouth" must affect the structure of the flow because *Stentor* causes a large flow at the membranelle (ciliary bands) around the anterior end (Figure 6-1). So, the flow field caused by *Stentor* was influenced by the geometries of the outer wall and the position of the anterior of the cell.

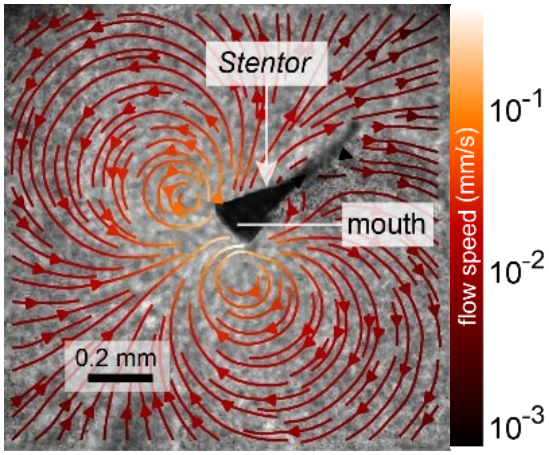

Figure 6-1 Flow field caused by adhering *S. coeruleus* in wide area.

Stentor attaches to the center of the image. Symmetrical vortex flow appears around the cell "mouth". The flow field is calculated by vector field obtained by PIV analysis using tracer particles. The colour of the line represents flow speed (log scale).

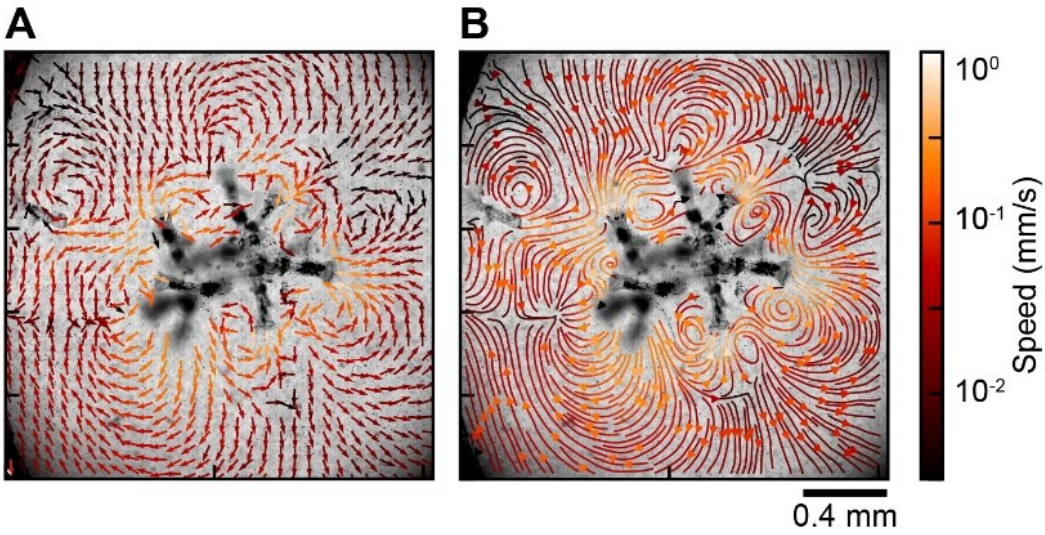

Figure 6-2 Flow field caused by colonysed *Stentor* sp. on the chamber.

They adhere to a substrate encouraged by a mucus secreted from the posterior region of the cell. In high cell concentrations, they form radial colonies, as shown in the centre of each image (A, B). The cooperative flow caused by each cell makes a complex structure of the flow vectors (A). From the vector field, the flow field is obtained (B). The colour represents a flow speed.

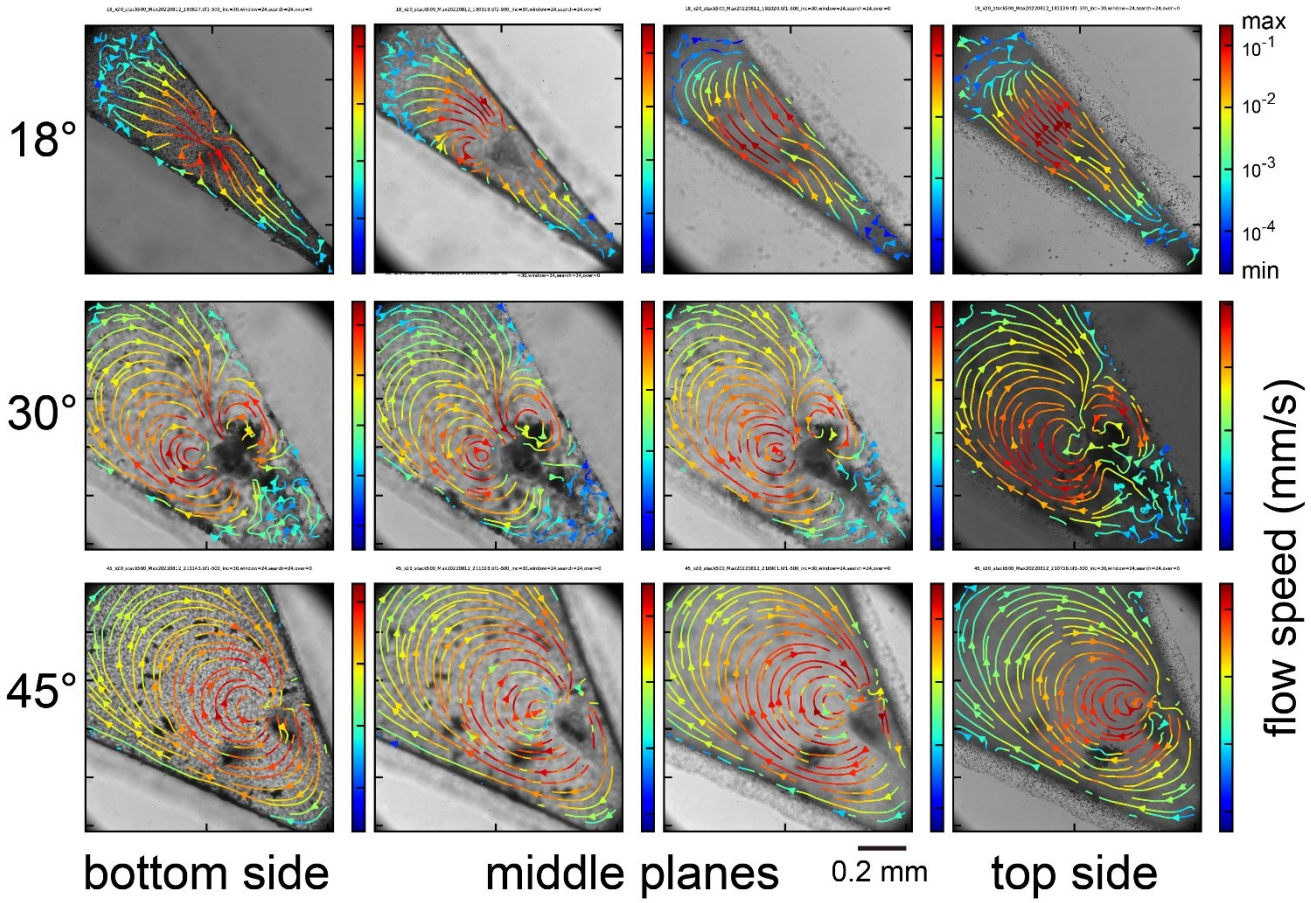

Figure 6-3 The flow fields according to the angle of corners and the focal plane.

In wide angles (30 and 45 degrees), the vortex flow is caused at the focal plane from the bottom to the top side of the chamber. In a narrow area (18 degrees), the flow comes in at the bottom side and out at the top side. So, we do not see vortex flow clearly. Colour represents a flow speed (log scale). Each scale is different. The maximum is the max speed, and the minimum is the minimum flow speed in each measurement.

6.2 The effect of medium viscosity about behavioral change

Next, I focus on the trigger of the behavioural transition from swimming to adhering. Before the adhering, the cell deforms to a trumpet shape. Then, I measured the proportion of the behavioural mode by observing the cell shapes. The frequency of the cell states was influenced by 1 % methylcellulose (Figure 6-4). Free swimming *S. coeruleus* took a swimming cone shape; conversely, the trumpet-shaped cell was dominant in the medium added methylcellulose. This viscosity of the methylcellulose is high compared to the culture medium. It indicates that the viscosity of the medium influences the states of the cell, and high viscosity changes its state from swimming to adhering.

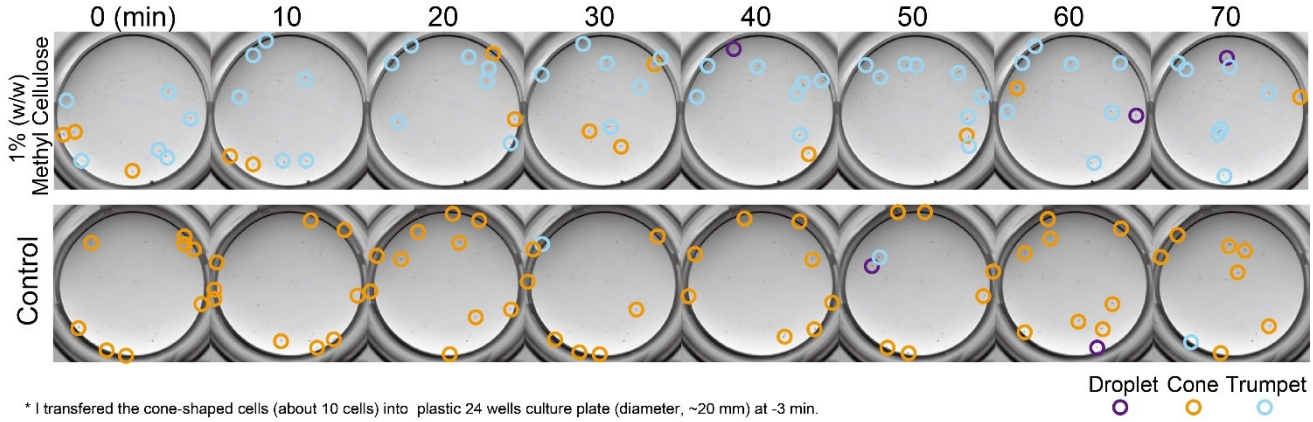

Figure 6-4 The influence of viscosity to the switching behaviour from swimming to adhering.

High viscosity influences the changing state from cone shape to trumpet shape. Time series of the cell's behaviour are shown and set up every 10 minutes. The cells are small due to low magnification. Colour circles represent three states.

6.3 Relationship between collision and behavioral change

From these results, *S. coeruleus* changes its states from a cone shape to a trumpet shape by a structure in the chamber, and most trumpet-shaped cells adhere to narrow areas formed by the structure and chamber's wall. Geometrical parameters forming observation chambers influence these selections. The question then arises as to the selection mechanism of anchoring locations in narrow areas. One possible explanation is that frequent collisions with structures affect their behavioural change because it is considered that the cell frequently contacts the wall in narrow spaces. In general, when swimming, *Stentor* enters a corner, and they behave backwards swimming (Figure 6-5) by performing ciliary reversal. Thus, to address this question, we observed the escaping behaviour in several narrow spaces formed by geometrical structures. Figure 6-6 and Figure 6-7 show the distribution of stucking time in each corner. From these distributions, the cell tended to get stuck and stay in narrower and sharper areas (Figure 6-8 and Figure 6-9). Figure 6-10 shows the difference in the time sequence of cell positions in the star chamber. We manually traced the outline of the cell at different times. In a low curvature area ($r = 0.25$), the cell remained swimming along the wall and then escaped from the area (Figure 6-10A).

On the other hand, we can see that the cell repeatedly changes the swimming direction back and forth at the tips in a high curvature area ($r = 0.06$, Figure 6-10B). We analyzed the number of reversals in the swimming direction per one escaping behaviour to quantify this behavioural difference depending on the extracellular geometry. The values were calculated by inner products of the swimming unit vectors at different frames using the positions of the cell centres. In narrower corners (30 and 45 degrees), the reversals of swimming direction significantly increased compared with broader areas (60 degrees) (Figure 6-11 and Figure 6-13A). In addition, the reversals in shaper corners ($r = 0.06$,

0.13) significantly increased compared with blunt corners (r = 0.25) (Figure 6-12 and Figure 6-13B). Backwards swimming is caused by ciliary reversal.

Moreover, we could observe backwards swimming in the reversal direction detected in this analysis. Therefore, the escaping behaviour differs depending on the angle and curvature forming the corner. It indicates that a high frequency of ciliary reversal caused by contact in the corner affects the behavioural transition from swimming to adhering.

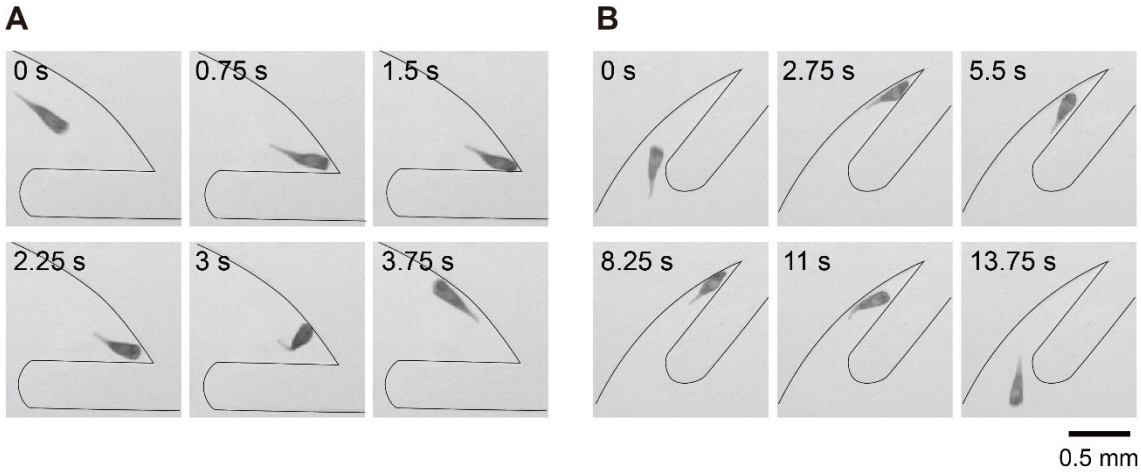

Figure 6-5 Typical sequential images of the process in the escaping behaviour from two corners.

Escaping behaviour in the 60-degree corner. The cell enters the corner after that it takes backward swimming and turns to escape from the corner. (B) Escaping behaviour in the 30-degree corner. The cell entering the corner repeatedly back and forth. After that it turns to other direction to escape. The time is shown at the upper left in each image.

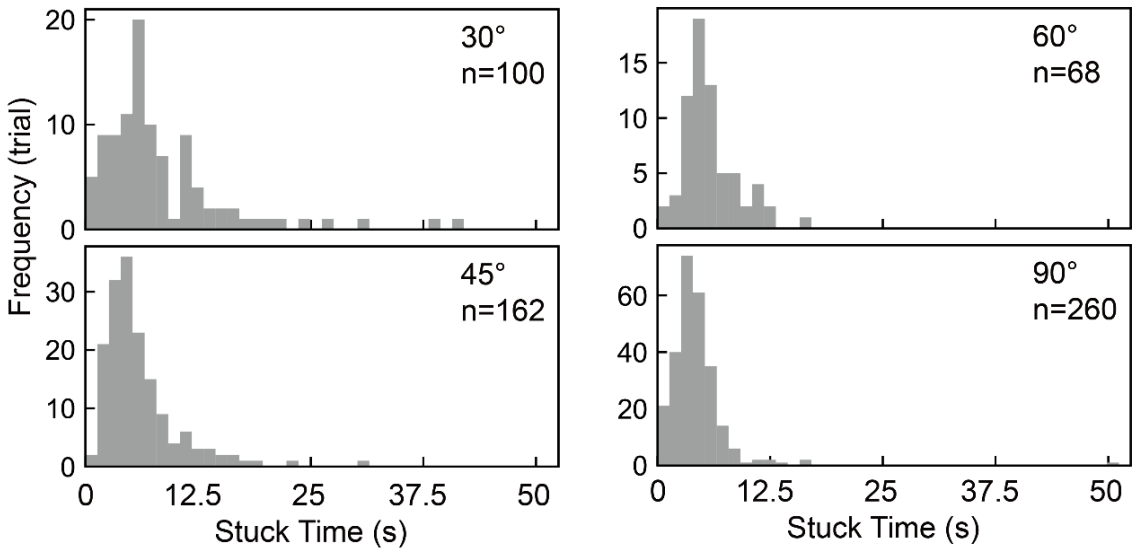

Figure 6-6 The distributions of duration time about stucking in each corner.

The corner angle and the number of stuck events are shown in the upper right of each graph. The graph shows the range from 0 s to 50 s.

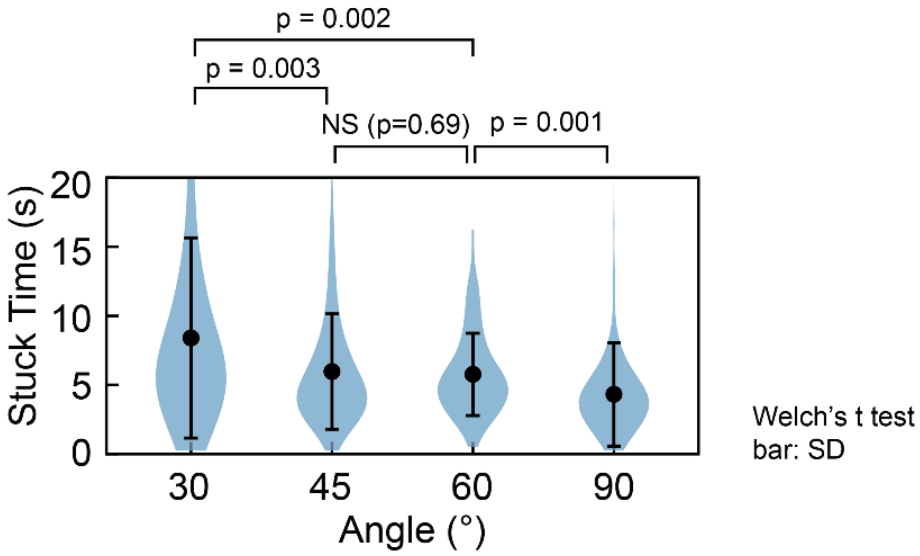

Figure 6-7 The comparison of stuck time in each corner.

Dots and bars are the mean value and standard deviations of duration times in Figure 6-6. Statistical analysis of Welch's t test conducted to this distribution.

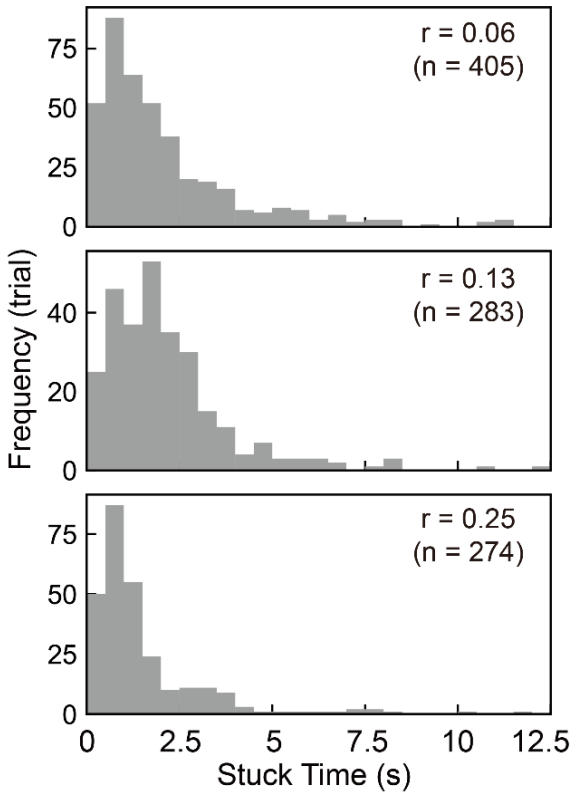

Figure 6-8 The distributions of duration time about stucking in each corner.

The corner curvature and the number of stuck events are shown in the upper right of each graph. The graph shows the range from 0 s to 12.5 s.

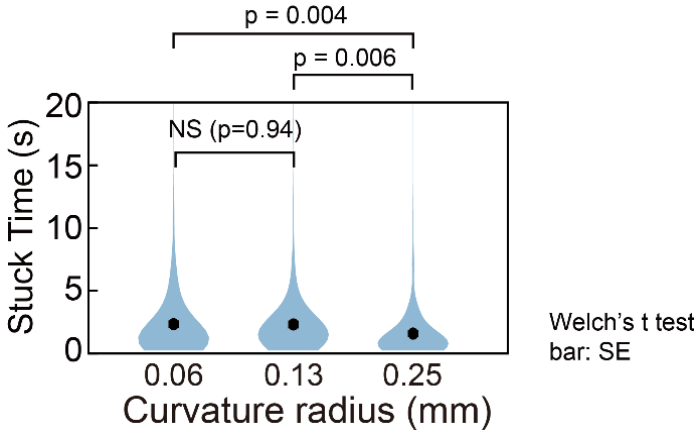

Figure 6-9 The comparison of stuck time in each corner.

Dots and bars are the mean value and standard deviations of duration times in Figure 6-8. Statistical analysis of Welch's t test conducted to this distribution.

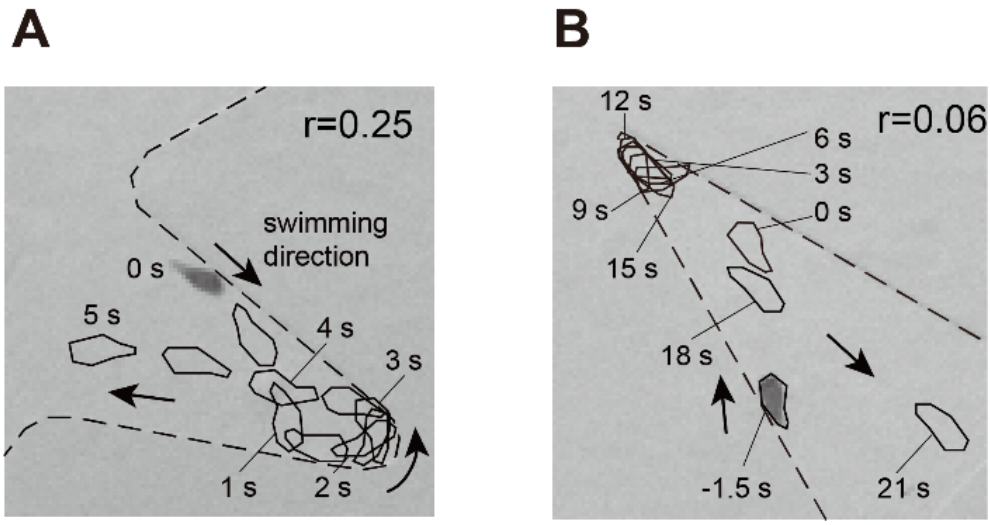

Figure 6-10 Time series of cell counter about two types of escaping behaviours in the corners.

In the smooth corner, the cell escapes by swimming along the wall. On the other hand, in sharp corners, the cell repeatedly reverses the ciliary beating at the corner tip.

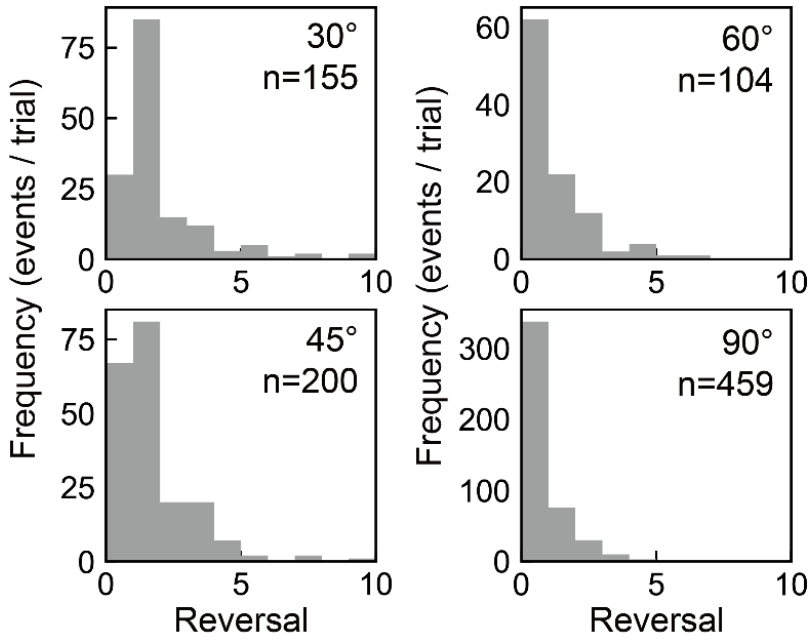

Figure 6-11 The distributions about the number of events that the cell reverses swimming direction per one trial in each corner.

The corner angle and the number of the entering corner are shown in upper right in each graph. The graph shows the range from 0 time to 10 times per one trial.

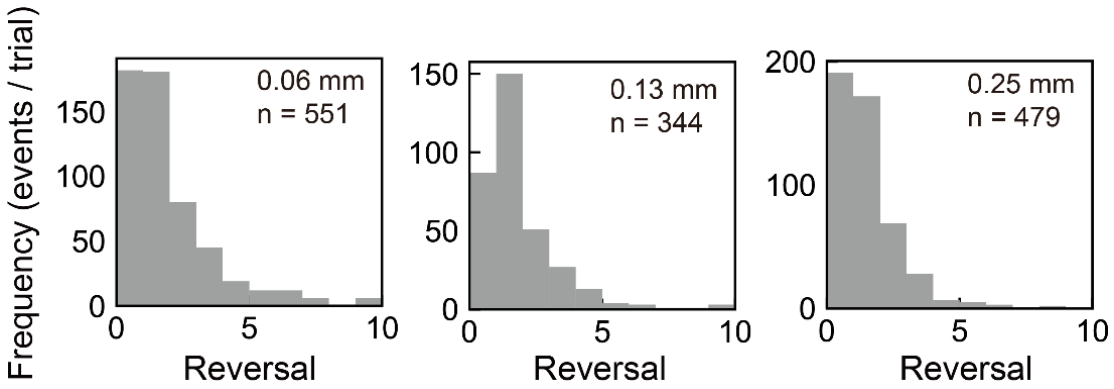

Figure 6-12 The distributions about the number of events that the cell reverses swimming direction per one trial in each corner.

The curvature radius and the number of entering corners are shown in the upper right of each graph. The graph shows the range from 0 times to 10 times per trial.

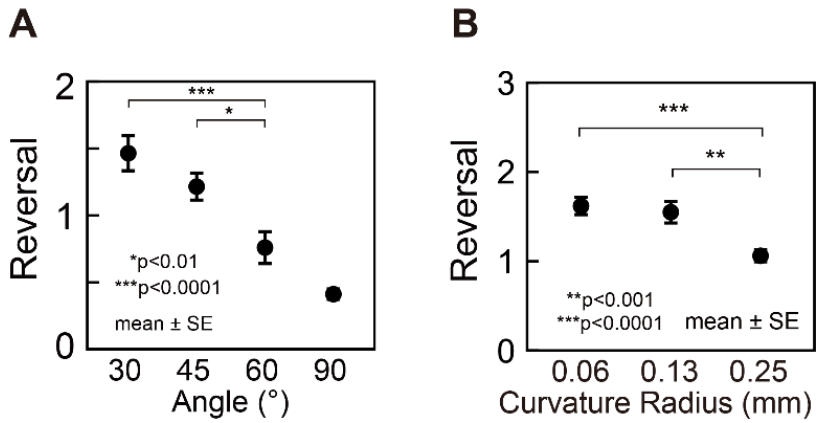

Figure 6-13 The comparison of the reversal of swimming direction in each corner.

Dots and bars are the mean value and standard errors of the reversal per one trial from Figure 6-11 and Figure 6-12. Statistical analysis of Welch's *t* test conducted to these distributions.

7 Discussions

7.1 Comparison between our experiments and previous research about behavioral change

Protists exhibit some behavioral modulations in response to their environments. The ciliate *Stentor* changes its shape and motility, and previous studies have highlighted the complexity of these behavioral transitions (Jennings, 1906; Wood, 1969; Dexter et al., 2019; Trinh et al., 2019). Environmental cues influence these behavioral transitions. Here, we quantitatively evaluated the behaviors of *S. coeruleus* and measured the characteristic durations of their behavioral transitions. By considering swimming speed and cell length, we computationally classified cell states into three types, consistent with the previous descriptive classification (Tartar, 1961). Among these states, we identified four transition processes in *S. coeruleus* accompanied by each characteristic duration time. Previous studies qualitatively estimated the duration of transitions from droplet to trumpet and from trumpet to droplet, and our results are consistent with these reports (Wood, 1970; Kristensen et al., 1974). The contraction process in *S. coeruleus* from trumpet to droplet contributes to the contractile filaments, named myoneme (Randall and Jackson, 1958; Huang and Pitelka, 1973) and *Vorticella convallaria* (Moriyama et al., 1998), which also uses a similar contractile filament, the spasmoneme (Lynn, 2008) is almost the same as that in *S. coeruleus*. Additionally, we characterized the duration of elongation processes from droplet to cone and from cone to trumpet. These elongation processes are associated with the sliding of microtubule ribbons in the km-fibers (Randall and Jackson, 1958; Huang and Pitelka, 1973). The duration times of three elongations were different suggesting that the question of intracellular mechanism in three elongation processes is still open.

In the transition from cone to trumpet, we observed a negative correlation between the cell length l and swimming speed s, following power laws of $s \sim l^{-6.3}$ and $s \sim l^{0.2}$ (Figure 4-6B). According to Stokes' law, in a moving sphere (radius r) with the same energy, the swimming speed is proportional to r^{-1}. The exponent between observed length and speed differs from that predicted by Stokes' law. This difference is likely due to variations in ciliary waveforms between the cone and trumpet states (Figure 4-9).

7.2 The trigger of behavioral change swimming to adhering

S. coeruleus has three types of form (droplet, cone, and trumpet), and surrounding environments modulate these states. Most cells take swimming cone states in the simple observation chamber without structure. On the other hand, the frequency of the trumpet shape increases in the chamber with a structure. Although the structure changes these frequencies in each state, there are many possible environmental changes, such as light or chemical effects created by the structures.

All experiments were conducted about light and chemical effects so that the cell sensitively performs photo-responses and behavioural changes by chemical substances. Before this observation, I transferred the cell to a fresh medium to prevent chemical effects. In particular, the cell reacts to green light (about 610 nm) in photophobic response and phototaxis accompanied by ciliary reversal (Song et al., 1980b; a). The cell's behaviour was recorded under uniformly weak red light to prevent these light effects. A swimming trajectory forms a straight spiral path in the cone-shaped cell, so the cell swims along the wall in the simple chamber. In the structural chamber, the swimming *Stentor* frequently collides with the obstacle from the front, and the cell behaves in ciliary reversal. It indicates frequent collision changes their states from cone-shaped swimming to trumpet-shaped adhering forms.

7.3 Behavioral change affected surrounding geometrical cues

Selecting behaviours in anchoring locations were observed in the chamber consisting of different narrow areas. Anchoring locations are affected by geometrical parameters about these narrow areas. What is the cause of its selection affected by geometrical cues? One possibility is that they are stuck in a narrow area because the stuck contributes to the high presence rate at some specific locations, and the adhering chance increases. In swimming states, the cell swims around these chambers, and presence rates in swimming cells were affected by geometrical parameters. It suggests that the stuck behaviour at the narrowness contributes to the bias of the selecting behaviours. If the cell randomly takes behavioural change from swimming to adhering, the presence rates in the swimming ultimately affect the frequencies of their anchoring. However, the standardisation of total adhering time by dividing the total presence time in the swimming cell at each corner also shows the bias of anchoring locations.

Moreover, I also standardise the total adhering time divided by the areas in each corner. Then, we can see the bias of the anchoring locations. This analysis indicates that other mechanisms, in addition to the stuck, contribute to the behavioural change from swimming to adhering modulated by geometrical cues.

Depending on the geometrical structures, the cell takes two escaping behaviours from narrow areas. When the cell enters a corner formed by the broad and rounded tip, the cell swims along the wall and escapes from this region. In the corners formed by a sharper tip and slight angle, the anterior of the cell repeatedly collides with the wall, and the cell frequently performs ciliary reversal. Although the side of the cell contacts when the cell swims along the wall, ciliary reversal occurs less. Previously, the contact angle to the wall in swimming ciliates and green algae affected the difference in escaping behaviour from the wall (Kantsler et al., 2013; Escoubet et al., 2023): the collision from the front produces a significant stimulus to the cell, and the cell reacts in ciliary reversal. Based on these

explanations, geometrical features of extracellular environments induce their ciliary reversal, and the cell may exhibit selecting anchoring location-influenced geometrical cues.

7.4 The benefit of adhering to narrow areas

Previously, a directional swimming organism such as *Chlamydomonas* accumulated in corners in the triagle chamber, and a phenomenon has been described as a theoretical model (Théry et al., 2021). While the cell accumulates in corners without changing the behavioural state (Mondal et al., 2021), we revealed that *S. coeruleus*, which is often found in a free-swimming form (Reynierse and Walsh, 1967), tended to adhere to chambers with structures promoting accumulation in crescent areas. In this behavior, the cell's anterior end faces the opposite side of the dead end. Hydrodynamically, *S. coeruleus*, classified as a puller-like swimmer in the squirmer model, tends to swim away from walls (Lighthill, 1952; Blake, 1971; Lauga and Powers, 2009). When the cell's posterior region, which secretes a sticky substance, attaches to a substrate (Andrews, 1945), the cell orients its anterior end toward the opposite side of the dead end, contributing to enhanced feeding efficiency.

Furthermore, Stentor is known to create two feeding vortices at the left and right sides of its oral apparatus on a focal plane (Maupas, 1888). Proximity to a surface or substrate induces vortex flow near sessile filter feeders like *Vorticella* and *Opercularia*, generating feeding currents around the oral apparatus similar to *Stentor* (Liron and Blake, 1981; Hartmann et al., 2007; Pepper et al., 2010, 2013). The feeding efficiency influenced by these feeding vortices depends on environmental conditions and theoretical definitions. Eddies contribute to decrease long-term feeding efficiency, defined by the clearance rate (the volume of nutrient water crossed per time) due to recirculation when assuming no nutrient in the flow passed through the oral region previously (Liron and Blake, 1981; Hartmann et al., 2007; Pepper et al., 2013, 2021). On the other hand, when we assume that the organisms probabilistically capture prey which pass through the oral region, the vortex array can increase feeding efficiency because recirculation enhances feeding chances, as observed in starfish larvae (Gilpin et al., 2017). Additionally, vortex flow enhances the mixing and transport of substances, i.e., nutrients and wastes, around the cell (Mondal et al., 2021). Combining our results with these reports, we suggest that S. coeruleus adheres to narrow areas to avoid becoming prey, capture prey, and enhance nutrient mixing, thus benefiting from the surrounding environment.

7.5 The mechanism of the behavioural change

What does the ciliary reversal effect on the behavioural change from swimming to adhering? In the above results, we see the influence of the obstacle regarding the behavioural change from a swimming cone shape to an adhering trumpet shape. Narrowness formed by a structure and chamber's wall increases the frequency of the collision. The frequency of ciliary reversal induced by mechanical stimuli depends on the surrounding geometrical features such as corner angle and

curvature. Thus, it indicates that geometrical structure contributes to the effect of selecting anchoring behaviour in *Stentor*.

On the surface of the cell, there are mechanoreceptor Ca ion channels (Wood, 1982). Mechanical stimuli influence the channels' opening and closing, and the cell takes the avoiding response as quick contraction by mechanical stimuli (Wood, 1969). In ciliary reversal in photoresponse, intracellular state such as membrane potential changes when the cell receives the light stimulus. Then, depolarization occurs, and a Ca^{2+} influx triggers a ciliary reversal (Song, 1981). The Ca influx depends on the geometrical features, and the chance of increasing Ca ion may increase in the region that the cell properly adheres to.

In ciliated protozoa, *Tetrahymena*, frequent collision to the wall regulates the mechanoreceptor channel and decreases the sensitivity of Ca ion (Kunita et al., 2016). The sensitivity decreases in the Ca ion channel, and the influx of Ca ion less occurs. It accompanies behavioural change; swimming trajectory modulates straight to high curvature. Based on its previous research, it considers that a *Stentor*, which undergoes frequent mechanical stimulation, causes less influx of Ca ion. So, intracellular Ca concentration may decrease. Ca-binding contractile protein, myoneme, runs just below the cell membrane (Randall and Jackson, 1958). The increase of Ca ion induces the quick contraction caused by myoneme. The adhering form is not contractile but has an elongated shape, so it is consistent with the cell's degradation of the Ca ion.

Some challenges to the measurement of intracellular conditions remain. It is hard to measure intracellular conditions. Previously, some electrophysiological research was done about measuring the membrane potential by injecting microelectrode (Naitoh and Eckert, 1969; Brette, 2021). However, the injection induces a significant mechanical stimulus for the cell (Escoubet et al., 2023). There are few studies about fluorescent measurement for Ca ion and membrane potential in *Paramecium* by injecting calcium indicator injecting Fluo-4 (Plattner, 2014). There are many studies about measuring Ca ion in mammals, not protists. So, it is challenging but important to reveal the intracellular mechanism of many protist behaviours. The relationship between the behaviours of protists and cellular mechanisms has been revealed by indirect measurements such as inhibitors or changing extracellular ion conditions (Song, 1981). Combining a quantification of behaviours and direct measurement of intracellular conditions contributes to understanding the simple strategy of unicellular organisms. In addition, Ca ions play a key role in biological reactions from unicellular to mammal. Quantifications of behaviour and direct measurements of intracellular states in protists will reveal biological mechanisms of a variety of complex unicellular behaviours.

8 References

Adl, S.M., D. Bass, C.E. Lane, J. Lukeš, C.L. Schoch, A. Smirnov, S. Agatha, C. Berney, M.W. Brown, F. Burki, P. Cárdenas, I. Čepička, L. Chistyakova, J. del Campo, M. Dunthorn, B. Edvardsen, Y. Eglit, L. Guillou, V. Hampl, A.A. Heiss, M. Hoppenrath, T.Y. James, A. Karnkowska, S. Karpov, E. Kim, M. Kolisko, A. Kudryavtsev, D.J.G. Lahr, E. Lara, L. Le Gall, D.H. Lynn, D.G. Mann, R. Massana, E.A.D. Mitchell, C. Morrow, J.S. Park, J.W. Pawlowski, M.J. Powell, D.J. Richter, S. Rueckert, L. Shadwick, S. Shimano, F.W. Spiegel, G. Torruella, N. Youssef, V. Zlatogursky, and Q. Zhang. 2019. Revisions to the classification, nomenclature, and diversity of eukaryotes. *J. Eukaryot. Microbiol.* 66:4–119. doi:10.1111/jeu.12691.

Adl, S.M., A.G.B. Simpson, M.A. Farmer, R.A. Andersen, O.R. Anderson, J.R. Barta, S.S. Bowser, G. Brugerolle, R.A. Fensome, S. Fredericq, T.Y. James, S. Karpov, P. Kugrens, J. Krug, C.E. Lane, L.A. Lewis, J. Lodge, D.H. Lynn, D.G. Mann, R.M. McCourt, L. Mendoza, O. Moestrup, S.E. Mozley-Standridge, T.A. Nerad, C.A. Shearer, A.V. Smirnov, F.W. Spiegel, and M.F.J.R. Taylor. 2005. The new higher level classification of eukaryotes with emphasis on the taxonomy of protists. *J. Eukaryot. Microbiol.* 52:399–451. doi:10.1111/j.1550-7408.2005.00053.x.

Adl, S.M., A.G.B. Simpson, C.E. Lane, J. Lukeš, D. Bass, S.S. Bowser, M.W. Brown, F. Burki, M. Dunthorn, V. Hampl, A. Heiss, M. Hoppenrath, E. Lara, L. Le Gall, D.H. Lynn, H. McManus, E.A.D. Mitchell, S.E. Mozley-Stanridge, L.W. Parfrey, J. Pawlowski, S. Rueckert, L. Shadwick, C.L. Schoch, A. Smirnov, and F.W. Spiegel. 2012. The revised classification of eukaryotes. *J. Eukaryot. Microbiol.* 59:429–493. doi:10.1111/j.1550-7408.2012.00644.x.

Andrews, E.A. 1945. Stentor's anchoring organs. *J. Morphol.* 77:219–232. doi:10.1002/jmor.1050770206.

Barry, J.P., and P.K. Dayton. 1991. Physical Heterogeneity and the Organization of Marine Communities. *In* Ecological Heterogeneity. J. Kolasa and S.T.A. Pickett, editors. Springer New York, New York, NY. 270–320.

Blake, J.R. 1971. A spherical envelope approach to ciliary propulsion. *J. Fluid Mech.* 46:199–208. doi:10.1017/S002211207100048X.

Blauch, L.R., Y. Gai, J.W. Khor, P. Sood, W.F. Marshall, and S.K.Y. Tang. 2017. Microfluidic guillotine for single-cell wound repair studies. *Proc. Natl. Acad. Sci. U. S. A.* 114:7283–7288. doi:10.1073/pnas.1705059114.

Bloodgood, R.A. 1981. Flagella-dependent gliding motility in *Chlamydomonas*. *Protoplasma*. 106:183–192. doi:10.1007/BF01275550.

Bondoc-Naumovitz, K.G., H. Laeverenz-Schlogelhofer, R.N. Poon, A.K. Boggon, S.A. Bentley, D. Cortese, and K.Y. Wan. 2023. Methods and Measures for Investigating Microscale Motility. *Integr. Comp. Biol.* 63:1485–1508. doi:10.1093/icb/icad075.

Brette, R. 2021. Integrative neuroscience of Paramecium, a 'swimming neuron'. *eNeuro*. 8. doi:10.1523/ENEURO.0018-21.2021.

Chang, R., and M. Prakash. 2023. Topological damping in an ultrafast giant cell. *Proc. Natl. Acad. Sci. U. S. A.* 120:e2303940120. doi:10.1073/pnas.2303940120.

Dacks, J.B., M.C. Field, R. Buick, L. Eme, S. Gribaldo, A.J. Roger, C. Brochier-Armanet, and D.P. Devos. 2016. The changing view of eukaryogenesis - fossils, cells, lineages and how they all come together. *J. Cell Sci.* 129:3695–3703. doi:10.1242/jcs.178566.

Dexter, J.P., S. Prabakaran, and J. Gunawardena. 2019. A complex hierarchy of avoidance behaviors in a single-cell eukaryote. *Curr. Biol.* 29:4323-4329.e2. doi:10.1016/j.cub.2019.10.059.

Echigoya, S., K. Sato, O. Kishida, T. Nakagaki, and Y. Nishigami. 2022. Switching of behavioral modes and their modulation by a geometrical cue in the ciliate *Stentor coeruleus*. *Front. Cell Dev. Biol.* 10:1021469. doi:10.3389/fcell.2022.1021469.

Eme, L., S.C. Sharpe, M.W. Brown, and A.J. Roger. 2014. On the age of eukaryotes: evaluating evidence from fossils and molecular clocks. *Cold Spring Harb. Perspect. Biol.* 6:a016139. doi:10.1101/cshperspect.a016139.

Escoubet, N., R. Brette, L.-L. Pontani, and A.M. Prevost. 2023. Interaction of the mechanosensitive microswimmer *Paramecium* with obstacles. *R. Soc. Open Sci.* 10:221645. doi:10.1098/rsos.221645.

Fenchel, T. 1982. Ecology of Heterotrophic Microflagellates. IV. Quantitative Occurrence and Importance as Bacterial Consumers. *Mar. Ecol. Prog. Ser.* 9:35–42.

Gilpin, W., V.N. Prakash, and M. Prakash. 2017. Vortex arrays and ciliary tangles underlie the feeding–swimming trade-off in starfish larvae. *Nat. Phys.* 13:380–386. doi:10.1038/nphys3981.

Gruber, A. 1878. Die Haftorgane der Stentoren. *Zool. Anz.* 1:390–391.

Hartmann, C., Ö. Özmutlu, H. Petermeier, J. Fried, and A. Delgado. 2007. Analysis of the flow field induced by the sessile peritrichous ciliate *Opercularia asymmetrica*. *J. Biomech.* 40:137–148. doi:10.1016/j.jbiomech.2005.11.006.

Hedges, S.B., J.E. Blair, M.L. Venturi, and J.L. Shoe. 2004. A molecular timescale of eukaryote evolution and the rise of complex multicellular life. *BMC Evol. Biol.* 4:2. doi:10.1186/1471-2148-4-2.

Huang, B., and D.R. Pitelka. 1973. The contractile process in the ciliate, *Stentor coeruleus*: I. the role of microtubules and filaments. *J. Cell Biol.* 57:704–728. doi:10.1083/jcb.57.3.704.

Inaba, F. 1959. Electron-microscope study on the fine structure of *Stentor coeruleus*. *Bull. Biol. Soc. Hiroshima Univ*. 10:35.

Ishikawa, T., and K. Kikuchi. 2018. Biomechanics of *Tetrahymena* escaping from a dead end. *Proceedings of the Royal Society B: Biological Sciences*. 285. doi:10.1098/rspb.2017.2368.

Iwatsuki, K. 1992. *Stentor coeruleus* shows positive photokinesis. *Photochem. Photobiol.* 55:469–471. doi:10.1111/j.1751-1097.1992.tb04264.x.

Iwatsuki, K., and P.-S. Song. 1989. The ratio of extracellular Ca^{2+} to K^{+} ions affects the photoresponses in *Stentor coeruleus*. *Comp. Biochem. Physiol. A Physiol.* 92:101–106. doi:10.1016/0300-9629(89)90749-4.

Jennings, H.S. 1902. Studies on reactions to stimuli in unicellular organisms. Ix.—on the behavior of fixed infusoria (Stentor and Vorticella), with special reference to the modifiability of protozoan reactions. *Am. J. Physiol.* 8:23–60. doi:10.1152/ajplegacy.1902.8.1.23.

Jennings, H.S. 1906. Behavior of the lower organisms. Columbia University Press, New York.

Kantsler, V., J. Dunkel, M. Polin, and R.E. Goldstein. 2013. Ciliary contact interactions dominate surface scattering of swimming eukaryotes. *Proc. Natl. Acad. Sci. U. S. A.* 110:1187–1192. doi:10.1073/pnas.1210548110.

Kapur, J.N., P.K. Sahoo, and A.K.C. Wong. 1985. A new method for gray-level picture thresholding using the entropy of the histogram. *Computer Vision, Graphics, & Image Processing*. 29:273–285. doi:10.1016/0734-189X(85)90125-2.

Kristensen, B.I., L.E. Nielsen, and J. Rostgaard. 1974. Variations in myoneme birefringence in relation to length changes in *Stentor coeruleus*. *Exp. Cell Res.* 85:127–135. doi:10.1016/0014-4827(74)90222-5.

Kunita, I., S. Kuroda, K. Ohki, and T. Nakagaki. 2014. Attempts to retreat from a dead-ended long capillary by backward swimming in *Paramecium*. *Front. Microbiol.* 5. doi:10.3389/fmicb.2014.00270.

Kunita, I., T. Yamaguchi, A. Tero, M. Akiyama, S. Kuroda, and T. Nakagaki. 2016. A ciliate memorizes the geometry of a swimming arena. *J. R. Soc. Interface*. 13:1–7. doi:10.1098/rsif.2016.0155.

Larson, B.T., J. Garbus, J.B. Pollack, and W.F. Marshall. 2022. A unicellular walker controlled by a microtubule-based finite-state machine. *Curr. Biol.* 32:3745-3757.e7. doi:10.1016/j.cub.2022.07.034.

Lauga, E., and T.R. Powers. 2009. The hydrodynamics of swimming microorganisms. *Rep. Prog. Phys.* 72:096601. doi:10.1088/0034-4885/72/9/096601.

Lewin, R.A. 1952. STUDIES ON THE FLAGELLA OF ALGAE. I. GENERAL OBSERVATIONS ON CHLAMYDOMONAS MOEWUSII GERLOFF. *Biol. Bull.* 103:74–79. doi:10.2307/1538407.

Lighthill, M.J. 1952. On the squirming motion of nearly spherical deformable bodies through liquids at very small reynolds numbers. *Commun. Pure Appl. Math.* 5:109–118. doi:10.1002/cpa.3160050201.

Liron, N., and J.R. Blake. 1981. Existence of viscous eddies near boundaries. *J. Fluid Mech.* 107:109–129. doi:10.1017/S0022112081001699.

Lynn, D.H. 2008. The Ciliated Protozoa. 3rd ed. Springer Netherlands., Dordrecht.

Marshall, W.F. 2021. Regeneration in *Stentor coeruleus*. *Front Cell Dev Biol*. 9:753625. doi:10.3389/fcell.2021.753625.

Martín-González, A., J. Wierzchos, J.C. Gutiérrez, J. Alonso, and C. Ascaso. 2008. Morphological stasis of protists in lower cretaceous amber. *Protist*. 159:251–257. doi:10.1016/j.protis.2007.08.006.

Maupas, E. 1888. Recherches experimentales sur la multiplication des infusoires cilies. *Archives de Zoologie Experimentale et Generale*. 46:498-516.

Moller, K.M. 1962. On the nature of stentorin. *C. R. Trav. Lab. Carlsberg*. 32:471–498.

Mondal, D., A.G. Prabhune, S. Ramaswamy, and P. Sharma. 2021. Strong confinement of active microalgae leads to inversion of vortex flow and enhanced mixing. *elife*. 10:1–23. doi:10.7554/eLife.67663.

Moriyama, Y., S. Hiyama, and H. Asai. 1998. High-speed video cinematographic demonstration of stalk and zooid contraction of *Vorticella convallaria*. *Biophys. J.* 74:487–491. doi:10.1016/S0006-3495(98)77806-3.

Müller, M., M. Mentel, J.J. van Hellemond, K. Henze, C. Woehle, S.B. Gould, R.-Y. Yu, M. van der Giezen, A.G.M. Tielens, and W.F. Martin. 2012. Biochemistry and Evolution of Anaerobic Energy Metabolism in Eukaryotes. *Microbiol. Mol. Biol. Rev.* 76:444–495. doi:10.1128/mmbr.05024-11.

Naitoh, Y., and R. Eckert. 1969. Ionic mechanisms controlling behavioral responses of *Paramecium* to mechanical stimulation. *Science*. 164:963–965. doi:10.1126/science.164.3882.963.

Newman, E. 1972. Contraction in *Stentor coeruleus*: A Cinematic Analysis. *Science*. 177:447–449. doi:10.1126/science.177.4047.447.

Ohmura, T., Y. Nishigami, A. Taniguchi, S. Nonaka, T. Ishikawa, and M. Ichikawa. 2021. Near-wall rheotaxis of the ciliate *Tetrahymena* induced by the kinesthetic sensing of cilia. *Science Advances*. 7. doi:10.1126/sciadv.abi5878.

Ohmura, T., Y. Nishigami, A. Taniguchi, S. Nonaka, J. Manabe, T. Ishikawa, and M. Ichikawa. 2018. Simple mechanosense and response of cilia motion reveal the intrinsic habits of ciliates. *Proc. Natl. Acad. Sci. U. S. A.* 115:3231–3236. doi:10.1073/pnas.1718294115.

Pedregosa, F., G. Varoquaux, A. Gramfort, V. Michel, B. Thirion, O. Grisel, M. Blondel, P. Prettenhofer, R. Weiss, V. Dubourg, J. Vanderplas, A. Passos, D. Cournapeau, M. Brucher, M. Perrot, and E. Duchesnay. 2011. Scikit-learn: Machine learning in Python. *J. Mach. Learn. Res.* 12:2825–2830.

Pepper, R.E., E.E. Riley, M. Baron, T. Hurot, L.T. Nielsen, M.A.R. Koehl, T. Kiørboe, and A. Andersen. 2021. The effect of external flow on the feeding currents of sessile microorganisms. *J. R. Soc. Interface*. 18:20200953. doi:10.1098/rsif.2020.0953.

Pepper, R.E., M. Roper, S. Ryu, P. Matsudaira, and H.A. Stone. 2010. Nearby boundaries create eddies near microscopic filter feeders. *J. R. Soc. Interface*. 7:851–862. doi:10.1098/rsif.2009.0419.

Pepper, R.E., M. Roper, S. Ryu, N. Matsumoto, M. Nagai, and H.A. Stone. 2013. A new angle on microscopic suspension feeders near boundaries. *Biophys. J.* 105:1796–1804. doi:10.1016/j.bpj.2013.08.029.

Plattner, H. 2014. Calcium regulation in the protozoan model, *Paramecium tetraurelia*. *J. Eukaryot. Microbiol.* 61:95–114. doi:10.1111/jeu.12070.

Rajan, D., T. Makushok, A. Kalish, L. Acuna, A. Bonville, K. Correa Almanza, B. Garibay, E. Tang, M. Voss, A. Lin, K. Barlow, P. Harrigan, M.M. Slabodnick, and W.F. Marshall. 2023. Single-cell analysis of habituation in *Stentor coeruleus*. *Curr. Biol.* 33:241-251.e4. doi:10.1016/j.cub.2022.11.010.

Randall, J.T., and S.F. Jackson. 1958. Fine structure and function in *Stentor polymorphus*. *J. Biophys. Biochem. Cytol.* 4:807–830. doi:10.1083/jcb.4.6.807.

Reynierse, J.H., and G.L. Walsh. 1967. Behavior modification in the protozoan *Stentor* re-examined. *Psychol. Rec.* 17:161–165. doi:10.1007/BF03393700.

Sanders, R.W., and S.A. Wickham. 1993. Planktonic protozoa and metazoa: predation, food quality and population control. *Mar. Microb. Food Webs*. 7:197–223.

Savikhin, S., N. Tao, P.S. Song, and W.S. Struve. 1993. Ultrafast pump-probe spectroscopy of the photoreceptor stentorins from the ciliate *Stentor coeruleus*. *J. Phys. Chem.* 97:12379–12386. doi:10.1021/j100149a045.

Sellner, K.G., G.J. Doucette, and G.J. Kirkpatrick. 2003. Harmful algal blooms: causes, impacts and detection. *J. Ind. Microbiol. Biotechnol.* 30:383–406. doi:10.1007/s10295-003-0074-9.

Shekhar, S., H. Guo, S.P. Colin, W. Marshall, E. Kanso, and J.H. Costello. 2023. Cooperative hydrodynamics accompany multicellular-like colonial organization in the unicellular ciliate *Stentor*. *bioRxiv*. 2023.01.10.523506. doi:10.1101/2023.01.10.523506.

Slabodnick, M.M., J.G. Ruby, S.B. Reiff, E.C. Swart, S. Gosai, S. Prabakaran, E. Witkowska, G.E. Larue, S. Fisher, R.M. Freeman Jr, J. Gunawardena, W. Chu, N.A. Stover, B.D. Gregory, M. Nowacki, J. Derisi, S.W. Roy, W.F. Marshall, and P. Sood. 2017. The Macronuclear Genome of *Stentor coeruleus* Reveals Tiny Introns in a Giant Cell. *Curr. Biol.* 27:569–575. doi:10.1016/j.cub.2016.12.057.

Song, P.-S. 1981. Photosensory transduction in *Stentor coeruleus* and related organisms. *Biochimica et Biophysica Acta (BBA) - Reviews on Bioenergetics*. 639:1–29. doi:10.1016/0304-4173(81)90002-1.

Song, P.-S. 1999. Photosensory signal transduction in *Stentor coeruleus*. *Journal of Photoscience*. 6:37–45.

Song, P.-S., D.-P. Häder, and K.L. Poff. 1980a. Step-up photophobic response in the ciliate, *Stentor coeruleus*. *Arch. Microbiol.* 126:181–186. doi:10.1007/BF00511225.

Song, P.-S., D.-P. Häder, and K.L. Poff. 1980b. Phototactic orientation by the ciliate, *Stentor coeruleus*. *Photochem. Photobiol.* 32:781–786. doi:10.1111/j.1751-1097.1980.tb04055.x.

Song, P.S., I.H. Kim, S. Florell, N. Tamai, T. Yamazaki, and I. Yamazaki. 1990. Structure and function of the photoreceptor stentorins in *Stentor coeruleus*. II. Primary photoprocess and picosecond time-resolved fluorescence. *Biochim. Biophys. Acta*. 1040:58–65. doi:10.1016/0167-4838(90)90145-6.

Tao, N., M. Orlando, J.S. Hyon, M. Gross, and P.S. Song. 1993. A new photoreceptor molecule from *Stentor coeruleus*. *J. Am. Chem. Soc.* 115:2526–2528. doi:10.1021/ja00059a068.

Tartar, V. 1961. The biology of *Stentor*. 58. Pergammon Press., New York.

de Terra, N. 1966. Culture of *Stentor coeruleus* on *Colpidium campylum*. *J. Protozool.* 13:491–492. doi:10.1111/j.1550-7408.1966.tb01947.x.

Théry, A., Y. Wang, M. Dvoriashyna, C. Eloy, F. Elias, and E. Lauga. 2021. Rebound and scattering of motile: *Chlamydomonas* algae in confined chambers. *Soft Matter*. 17:4857–4873. doi:10.1039/d0sm02207a.

Trinh, M.K., M.T. Wayland, and S. Prabakaran. 2019. Behavioural analysis of single-cell aneural ciliate, *Stentor roeseli*, using machine learning approaches. *J. R. Soc. Interface*. 16:20190410. doi:10.1098/rsif.2019.0410.

Walker, E.B., T.Y. Lee, and P.S. Song. 1979. Spectroscopic characterization of the stentor photoreceptor. *Biochimica et Biophysica Acta (BBA) - General Subjects*. 587:129–144. doi:10.1016/0304-4165(79)90227-7.

Wan, K.Y., and G. Jékely. 2021. Origins of eukaryotic excitability. *Philos. Trans. R. Soc. Lond. B Biol. Sci.* 376:0–2. doi:10.1098/rstb.2019.0758.

Wood, D.C. 1969. Parametric studies of the response decrement produced by mechanical stimuli in the protozoan, *Stentor coeruleus*. *J. Neurobiol.* 1:345–360. doi:10.1002/neu.480010309.

Wood, D.C. 1970. Electrophysiological studies of the protozoan, *Stentor coeruleus*. *J. Neurobiol.* 1:363–377. doi:10.1002/neu.480010402.

Wood, D.C. 1976. Action spectrum and electrophysiological responses correlated with the photophobic response of *Stentor coeruleus*. *Photochem. Photobiol.* 24:261–266. doi:10.1111/j.1751-1097.1976.tb06821.x.

Wood, D.C. 1982. Membrane permeabilities determining resting, action and mechanoreceptor potentials in *Stentor coeruleus*. *J. Comp. Physiol. A Neuroethol. Sens. Neural Behav. Physiol.* 146:537–550. doi:10.1007/bf00609450.

Wood, D.C. 1988. Habituation in *Stentor*: produced by mechanoreceptor channel modification. *J. Neurosci.* 8:2254–2258. doi:10.1523/jneurosci.08-07-02254.1988.

Wood, D.C. 1989. Localization of mechanoreceptors in the protozoan, *Stentor coeruleus*. *Journal of Comparative Physiology A*. 165:229–235. doi:10.1007/BF00619197.

Zhang, J., W. Qin, C. Hu, S. Gu, X. Chai, M. Yang, F. Zhou, X. Wang, K. Chen, G. Yan, G. Wang, C. Jiang, A. Warren, J. Xiong, and W. Miao. 2023. Giant proteins in a giant cell: Molecular basis of ultrafast Ca^{2+}-dependent cell contraction. *Sci Adv*. 9:eadd6550. doi:10.1126/sciadv.add6550.

Zhang, K.S., L.R. Blauch, W. Huang, W.F. Marshall, and S.K.Y. Tang. 2021. Microfluidic guillotine reveals multiple timescales and mechanical modes of wound response in *Stentor coeruleus*. *BMC Biol.* 19:1–17. doi:10.1186/s12915-021-00970-0.

9 Acknowledgement

I conducted these studies with Prof. Toshiyuki Nakagaki, Prof. Osamu Kishida, Prof. Katsuhiko Sato and Prof. Yukinori Nishigami. I would like to thank Prof. Takuji Ishikawa and Prof. Kenta Ishimoto for useful discussions. I am grateful to Prof. Jian Ping Gong and Prof. Shinji Nakaoka for taking charge of the sub-chief examiner. These works were supported by the Sasakawa Scientific Research Grant from The Japan Science Society Grant No. 2021-6029, the establishment of university fellowships towards the creation of science technology innovation, Grant Number JPMJFS2101, JSPS KAKENHI (JP21H05310) and The Sumitomo Foundation Fiscal 2023 Grant for Basic Science Research Projects (2300464).